



JGR Solid Earth

RESEARCH ARTICLE

10.1029/2019JB018749

Special Section:

Physical Properties of Rocks, Friction and Fracturing: The Walsh Volume

Key Points:

- Plastic faulting is nucleated by weakness associated with local structural alteration under conditions of severe plastic deformation
- Plastic faulting in ice does not require phase transformation and is sometimes inconsistent with the precepts of transformational faulting
- All solids may have the capacity for plastic faulting; that it is recognized in so few may reflect the extreme nature of requisite conditions

Supporting Information:

- Supporting Information S1

Correspondence to:

W. B. Durham,
wbdurham@mit.edu

Citation:

Golding, N., Durham, W. B., Prior, D. J., & Stern, L. A. (2020). Plastic faulting in ice. *Journal of Geophysical Research: Solid Earth*, 125, e2019JB018749.
<https://doi.org/10.1029/2019JB018749>

Received 24 SEP 2019

Accepted 6 FEB 2020

Accepted article online 7 FEB 2020

Plastic Faulting in Ice

N. Golding¹, W. B. Durham¹ , D. J. Prior² , and L. A. Stern³

¹Earth, Atmospheric and Planetary Sciences Department, Massachusetts Institute of Technology, Cambridge, MA, USA,

²Department of Geology, University of Otago, Dunedin, New Zealand, ³U.S. Geological Survey, Menlo Park, CA, USA

Abstract Plastic faulting is a brittle-like failure phenomenon exhibited by water ice and several other rock types under confinement. It is suspected to be the mechanism of deep earthquakes and extreme cases of shear localization in shallow rocks. Unlike ordinary Coulombic failure, plastic faulting is characterized by a pressure-independent failure strength and fault plane oriented 45° to maximum principal stress. To research the question of how the instability initiates, we conducted over 50 constant-displacement-rate experiments on polycrystalline ice (phases Ih and II) near the brittle-to-ductile (B-D) transition, at confining pressures $P = 0\text{--}300$ MPa, applied strain rates $\dot{\varepsilon} = 5 \times 10^{-5} - 7 \times 10^{-3}$ s $^{-1}$, temperatures $T = 105\text{--}233$ K, and mean grain sizes $d = 0.25\text{--}1.18$ mm. We find that (1) the width of the B-D transition in variable space is vanishingly narrow, to the point of appearing as a crossover, (2) a plastic fault plane, once formed, is not a zone of subsequent weakness, (3) distributed ice I \rightarrow II phase transformation in small amounts (<1 vol%) shows no causal relationship to subsequent failure, and (4) plastic faulting also occurs in ice II. We hypothesize that the elusive nucleating “trigger” parallels that of metals and ceramics undergoing severe plastic deformation, wherein transient local structural rearrangement occurs, in turn causing material strength to drop to a level sufficiently low, in a volume sufficiently large, that adiabatic instability is nucleated. Our results do not require and often are inconsistent with phase transformation. Plastic faulting may therefore be available to all solids undergoing severe deformation, and its appearance in so few is simply the result of insufficiently extreme conditions.

1. Introduction and Background

Ice Ih exhibits two distinct modes of brittle failure when loaded in triaxial compression (Durham et al., 1983; Kirby et al., 1991; Renshaw & Schulson, 2004; Schulson, 2002). Under low but nonzero levels of confining pressure, brittle failure is characterized by the development of a macroscopic shear fault composed of gouge material and a wide zone of coalesced microcracks, oriented following the dictates of the Mohr-Coulomb relationship at a steep angle (often within 30°) to the direction of maximum compression. This mode of failure, called Coulombic or frictional faulting, is associated with pressure strengthening, increased dilatancy near failure, and a low degree of cohesion. The mechanism governing this mode of failure in ice has previously been discussed in terms of crack mechanics, where frictional sliding on primary inclined cracks drives a process zone at crack tips, with that zone involving out-of-plane initiation, growth, and interaction of secondary cracks via the comb-crack mechanism (Renshaw & Schulson, 2001; Schulson, 1999). Coulombic faulting is the most common mechanism of brittle failure of most crystalline rock types in Earth’s shallow crust (e.g., Paterson, 1978).

At pressures above a few tens of MPa, however, hexagonal ice Ih (hereafter simply ice I) exhibits a mode of brittle failure called plastic faulting, which has been seen in only a few other rock types (Durham et al., 1983). Plastic faulting involves the same sudden and substantial loss of strength that characterizes Coulombic faulting but differs in that pressure strengthening and dilatancy, so prominent in the Coulombic process, are absent; and the fault plane, when it is possible to observe, is oriented at ~45° to the direction of maximum compression, on a plane of maximum shear stress. The absence of dilatancy means that microfracturing is absent, that is, that the plastic faulting mechanism is fundamentally a shearing process. In ice, where the process has been studied most thoroughly, the fault is observed to retain a high degree of cohesion, and the material within the fault is highly strained and usually composed of recrystallized grains, often of very fine grain size (Golding et al., 2012; Kirby et al., 1991; Rist & Murrell, 1994).

Adapting an already ambiguous geomaterials science lexicon to the discussion of plastic faulting, a process with an oxymoronic name that is seemingly inconsistent with the norms of rock mechanics, requires clarification of two potentially ambiguous terms important to this paper: “brittle” and “failure.” We use “brittle” to describe a mode of stress-strain behavior characterized by sudden or catastrophic loss in strength accompanied by inelastic displacement localized on a narrow fault plane or planes, and “failure” as the inability to support a load without deforming inelastically. Importantly, as used here, neither term is meant to imply a physical deformation mechanism such as localized cracking or distributed ductility. Thus, we can say that plastic faulting is a mode of brittle failure and that rocks can fail in either brittle or ductile fashion.

Plastic faulting appears in both warm ice, $T = 233\text{--}263\text{ K}$ (Rist et al., 1994; Rist & Murrell, 1994; Sammonds et al., 1998), and cold ice, $T = 77\text{--}158\text{ K}$ (Durham et al., 1983; Kirby et al., 1987). The plastic faulting phenomenon occurs during working of certain metals and ceramics, even at cryogenic temperatures (e.g., Rogers, 1979), and in laboratory testing of certain materials other than ice, including the germanate analog to olivine, Mg_2GeO_4 (Burnley et al., 1991; Schubnel et al., 2013), and the hydrous mineral serpentine (Meade & Jeanloz, 1991; Renshaw & Schulson, 2017). It is an important geological process in that it is widely speculated to be the mechanism of deep earthquakes (e.g., Hobbs & Ord, 1988; Regenauer-Lieb & Yuen, 2003; Schubert et al., 1975) and of certain shallow crustal earthquakes (Duretz et al., 2015).

Schulson (2002) showed that localization of displacement on a single narrow plane in ice I by mechanisms that are entirely ductile can be described by general relationships governing adiabatic shear instability. Localization of shear strain (“shear zones”) is an expression of deformation common in systems containing feedback loops (e.g., Regenauer-Lieb & Yuen, 2003). In particular, feedbacks between temperature, material strength, and plastic work can cause temperature and strain rate to rise virtually without limit if the heat of plastic work cannot be dissipated faster than it is generated (Golding et al., 2012; Karato et al., 2001; J. P. Poirier, 1980; Rogers, 1979). Strain softening following a maximum in the stress-strain curve can also cause localization and thus has the potential to catalyze adiabatic shear instability (Schulson, 2002; Semiatin et al., 1984).

Examples of localization in geologic systems grade from distributed deformation to narrow shear bands. In most such settings strain rates are low and strains high, and the development of localization can be plausibly rationalized in terms of feedback coupling of known (or approximately known) physical properties and processes (e.g., Duretz et al., 2015; Regenauer-Lieb & Yuen, 2003; Warren & Hirth, 2006). Tracing the physical origins of catastrophic adiabatic instability, however, is more problematic because of the short time scales involved. There has been some success in metals. Adiabatic shear instability is widely recognized in metals deformed under extreme conditions (often called “severe plastic deformation”) in serrated yielding, equal channel angular processing, high-speed penetration, etc. The nuclei of instability have been established to be zones of microstructural refinement, usually by recrystallization to nanosize grains, with resultant rheological weakness and focusing of plastic flow (Kula & DeSisto, 1966; Meyers et al., 2006; Murr et al., 2002; Rittel et al., 2008). Rist et al. (1994) reasonably concluded that the nucleating process for plastic faulting in ice I must involve localized plasticity but could only speculate about the origin of such weakness.

Leading hypotheses for the triggering mechanism of earthquakes deeper than the shallow crust include “transformational faulting” under phase-metastable conditions, wherein the volume collapse of the olivine-spinel transformation creates local conditions of severe plastic deformation (Kirby et al., 1991), whose grain-size reduction may be facilitated by the reconstructive phase transformation (Green & Burnley, 1989); dehydration and the reduction of effective pressure by the release of water (Meade & Jeanloz, 1991); adiabatic transformational faulting under phase-stable conditions induced by local shear heating across an equilibrium phase boundary (Renshaw & Schulson, 2017); and local melting (Griggs & Handin, 1960; Li et al., 2018). Importantly, for this paper, transformational faulting has also been hypothesized as the mechanism behind plastic faulting in ice observed in the laboratory (Kirby et al., 1991, 1992), given the proximity of test conditions to the ice I/II univariant phase boundary, the large volume decrease accompanying transformation ($>25\%$), and the direct observation of ice II in samples after testing. The olivine \rightarrow spinel and ice I \rightarrow II phase transformations share one other important property that makes the transformational faulting hypothesis attractive, namely, significant kinetic inhibition, allowing pressurization without phase change well beyond the equilibrium phase boundary and the possibility of

catastrophic release of stored elastic energy when phase change does occur. The low- to high-pressure phase transformation induced by overpressurization in olivine at cool temperatures has high nucleation rates and low growth rates, creating a fine-grained and therefore rheologically weak daughter phase (Rubie & Ross, 1994) that can shear at explosive rates (Burnley et al., 1991; Green & Burnley, 1989). Renshaw and Schulson (2017) speculated that during adiabatic transformational faulting, fault propagation is effected through transformational superplasticity, that is, transient structural weakness in the volume currently undergoing phase transformation, which leads to repeated cycles of local heating and operation of the adiabatic trigger.

Early experimental studies of the flow behavior of individual high-pressure ice phases and of ice undergoing high-pressure phase transformation, which eventually led to the discovery of the plastic faulting phenomenon in ice, were originally motivated by planetary interests (Durham et al., 1983; Echelmeyer & Kamb, 1986; J.-P. Poirier et al., 1981). Phase transformation even under geologic strain rates is likely to influence the internal dynamics and structure of the several large icy moons in the outer solar system (e.g., McKinnon, 1998) and of putative super-Earth “water planets” (e.g., Fu et al., 2010). However, the planetary application of plastic faulting may be tenuous. Stresses required for plastic faulting in ice are generally far higher than can be supported in most natural settings, so widespread occurrence of the phenomenon in nature might not be expected. Application to meteoritic impact events cannot be discounted, however, where flow and fracture properties of ice may influence the character of ejecta deposits, among other observables (Melosh, 1989; Singer et al., 2013).

Here we present experimental results on the mechanical and structural characteristics of plastic faulting in ice at intermediate temperatures, $T = 105\text{--}220\text{ K}$, thus bridging a gap between previous low- and high-temperature observations. Our aim is to understand in more detail the physics of plastic faulting in ice. Our strategy is to focus on behavior near the transition from unstable failure by plastic faulting to stable failure by distributed ductility (i.e., creep), akin to the brittle-to-ductile transition in crustal rocks (see review by Evans et al., 1990). Although plastic faulting in ice is probably not widespread in nature, given the high levels of deviatoric stress involved, such conditions are easily accessed in the laboratory, making ice ideal for laboratory study of the process because of its availability and the ease with which samples of desired initial grain textures can be fabricated.

2. Methods

The procedures summarized here build on those described in Durham et al. (1983) and Stern et al. (1997) for experimental deformation and for sample fabrication, respectively.

2.1. The Ice

Cylindrical specimens of polycrystalline ice I with diameter 25.4 mm and length 50–65 mm were fabricated as follows: Sieved ice grains ground from frozen, bubble-free, deionized water were packed into cylindrical stainless-steel molds to a pore volume of 40%. Three sizes of sieved grains were used in the present work: 0.18–0.25, 0.50–1.00, and 1.00–2.00 mm. The molds were then evacuated to approximately 100 Pa and then submerged in an agitated ice-water bath at $T = 273\text{ K}$ for 45 min. While still under vacuum, the molds were then flooded with deionized, deaerated water, also at $T = 273\text{ K}$. After flooding, the ice-water molds were subjected to unidirectional solidification from the bottom upward at $T = 243\text{ K}$. The resulting ice I was free from cracks and semitransparent, with a porosity of less than 0.5% (based on measured weight and dimensions, using a grain density of $920.0\text{ kg}\cdot\text{m}^{-3}$ at $T = 243\text{ K}$; Petrenko & Whitworth, 1999). Using scanning electron microscope electron backscatter diffraction (SEM-EBSD) and optical thin sections, final grain size was determined to be $d = 0.25 \pm 0.10\text{ mm}$, $d = 0.68 \pm 0.23\text{ mm}$, and $d = 1.18 \pm 0.41\text{ mm}$, respectively, for the three seed sizes used here, where grain size is the diameter of a circle of equivalent area as measured by EBSD and grains are segmented using a threshold misorientation of 10° using the MTEX code of Bachmann et al. (2011). EBSD imaging also confirmed that the grains exhibited no preferential orientation and were free from internal strain.

Prior to testing, specimens were encapsulated and sealed in pressure-tight, thin-walled (0.5 mm) indium jackets, which conform tightly to the underlying sample surface once the assembly is pressurized (Figure 1). Jacketed assemblies included 12.7-mm-long stainless-steel end caps at either end and a 19-

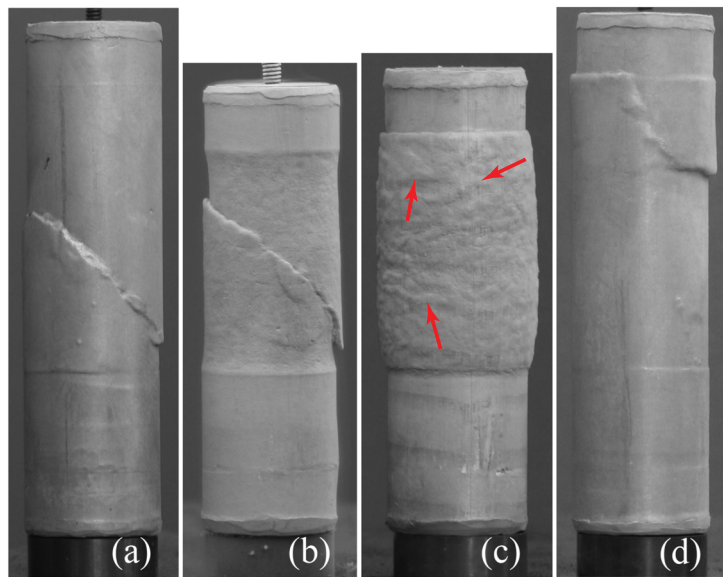


Figure 1. Postfailure appearance of ice samples representative of four types of behavior. Sample assemblies are in the nonventing configuration (Figure S1) wherein the cylindrical ice sample is bounded at top and bottom by hard end plugs and the assembly encapsulated in a 0.5-mm-thick indium jacket. Indium is much weaker than ice, so that under pressure, it conforms tightly to the sample surface and replicates in good detail surface features on the underlying ice sample, as is evident here. Loading direction is vertical. Starting sample lengths were approximately the same for all four. For scale, the dark pedestal beneath each assembly is 25 mm in diameter. (a) Plastic faulting, ice I (run 701), characterized by a single through-going fault inclined at 45° to the loading axis, with no other deformation apparent in the image. (b) Plastic faulting, ice II (run 746), characterized by a single fracture also inclined at 45° to load. Ice II sample volume is reduced by ~25%. (c) Ductile failure, ice I. Arrows indicate examples of jacket rumpling. (d) Coulombic failure, ice I (run 698), tested at a very low confining pressure of 3 MPa, characterized by an irregular fault that is in part more steeply inclined than the plastic fault.

mm-long zirconia disc between ice and end cap at one of the ends, which served as a thermal insulator during assembly (see Figure S1 in the supporting information). Care was taken during assembly to prevent sudden changes in temperature to avoid thermal fractures in the ice. Assembly ends were maintained parallel within 0.1°.

Polycrystalline ice II was fabricated through high-pressure phase transformation from ice I to ice II. Specimens of ice I with starting grain size $d = 0.68$ mm were loaded at $T = 200$ K to a hydrostatic confining pressure of $P \approx 300$ MPa at a rate of 20 to 30 MPa min $^{-1}$ (note that the symbol P in this paper refers strictly to gas pressure and is different from mean stress, the trace of the stress tensor, when the state of stress includes a nonzero deviatoric component). Under these conditions, the ice I→II transformation occurred at a confining pressure of $P \approx 240$ MPa. X-ray diffraction of earlier samples transformed in similar manner reveals that the I→II transformation runs to near completion, with no recognizable ice I diffraction peaks, with a resolution of ~2 vol% (Durham et al., 1988). To realign specimen ends after the phase transformation, an axial differential stress of $\sigma \approx 20$ MPa was applied for ~10 min at $T = 200$ K. After transformation, the temperature was reduced to $T = 105\text{--}110$ K over a period of ~6 hr before mechanical testing. At all times, P was maintained within the ice II stability field. Based on prior analysis by Kubo et al. (2006), the resulting ice II grain size is expected to be on the order of $d = 25\text{--}50$ μm .

2.2. Experimental Procedure

Axisymmetric compression tests were performed in our high-pressure cryogenic deformation apparatus (Heard et al., 1990) (see also Figure S1). Axial stress σ_1 was applied using a screw-driven piston advancing at constant displacement rate. Differential stress, the difference between the maximum and minimum principal compressive stresses, $\sigma = \sigma_1 - P$ (since $\sigma_2 = \sigma_3 = P$), was determined from the piston load, measured by a force gage internal to the pressure vessel (Figure S1), normalized by specimen cross-sectional area. Axial load and piston displacement were recorded digitally at coarse time interval (~7 s) and with an analog chart

Table 1
Summary of Ductile Runs, Ice I

Run	<i>d</i> (mm)	<i>T</i> (K)	<i>P</i> (MPa)	$\dot{\varepsilon}$ (s^{-1})	σ_{ult} (MPa)	σ_{ss} (MPa)	ε total	Hyperlink to		
								Photo	Chart ^e	Log
672	0.25	200	28	3.8×10^{-4}	79.9	49.2	0.26	672p	n/a	672b
675 ^a	0.25	200	30	3.3×10^{-3}	92.1	0.142		675p	675c	675b
677	0.25	195	25	5.0×10^{-4}	93.2	59.0	0.054	677p	677c	677b
681	0.68	233	18	6.2×10^{-3}	53.0	35.0	0.236	681p	n/a	681b
686	0.68	220	20	5.6×10^{-3}	67.7	37.9	0.192	686p	n/a	686b
699	0.68	180	100	5.7×10^{-4}	108.0	86.8	0.071	699p	699c	699b
706	0.68	180	200	3.5×10^{-3}	86.6	56.7 ^b	0.222	706p	706c	706b
710	0.68	180	200	2.9×10^{-3}	100.7	61.9 ^b	0.224	710p	710c	710b
711	0.68	180	100	5.4×10^{-5}	82.1	63.0	0.222	711p	711c	711b
712	0.68	180	100	7.1×10^{-4}	106.7	91.2	0.145	712p	712c	712b
716	0.25	180	50	5.8×10^{-4}	111.0	89.9	0.133	716p	716c	716b
723	1.18	180	50	1.0×10^{-4}	93.9 ^c	71.1	0.071	723p	723c	723b
725	0.68	180	50	5.4×10^{-5}	88.2	66.5	0.173	725p	725c	725b
727	0.68	180	50	2.0×10^{-4}	101.3	78.9	0.149	727p	727c	727b
729	0.68	180	150	1.0×10^{-3}	104.9	86.7	0.203	729p	729c	729b
739(1) ^d	0.68	180	50	1.0×10^{-4}	93.4	78.1	0.045	739(1)p	739(1)c	739(1)b
740(1) ^d	0.68	180	50	1.3×10^{-4}	95.2	75.2	0.065	740(1)p	740(1)c	740(1)b

^aUsed vented sample assembly (see Figure S1). ^bSignificant phase transformation occurred during run. Value is that of minimum differential stress during transformation. ^cDistinct blip at 91.5 MPa before peak stress. ^dStep (2) in Table 2. ^eLink to guide for reading strip charts.

recorder to capture the point of brittle failure more precisely (0.1 to 1 s, depending on chart speed). At fixed displacement rate, load on a specimen will increase until it can no longer be supported, at which point the specimen fails (in the sense defined in section 1). Failure may be brittle, where the specimen loses all or most of its mechanical integrity very rapidly, or may be controlled (ductile failure), wherein the specimen maintains much or all of its strength as deformation continues. In both cases, the peak value of σ achieved is called the ultimate strength, σ_{ult} . Strain rate $\dot{\varepsilon}$ was calculated as an engineering strain (or shortening) rate equal to piston displacement rate normalized by initial specimen length. Likewise, the magnitude of inelastic (i.e., nonrecoverable) strain ε was measured as piston displacement normalized by initial specimen length less the elastic component, which in turn was calculated from the known compliance of the deformation column and the current load. Differential stress was measured with a sensitivity better than ± 0.1 MPa. Hydrostatic confining pressure using nitrogen gas as a confining medium was generated using a conventional oil-gas separator/intensifier system and was measured using a Heise Bourdon tube gage. Compressive stresses and strains are taken here as positive.

For testing at 170 K and above, temperature was maintained by circulating liquid nitrogen in Cu tubing through a 30-L alcohol bath. Because of the large mass of the cryostat and pressure vessel, temperature variations during testing were small, typically less than ± 0.1 K. Temperature was measured with type J and type K thermocouples with accuracy of roughly ± 1.5 K. For deformation tests at $T < 170$ K, liquid nitrogen was released directly into the cryostat without alcohol present. For these tests, a larger temperature gradient existed across the cryostat, corresponding to an accuracy of ± 3 K.

3. Experiments: Results and Analysis

We performed over 50 constant displacement rate, axisymmetric compression tests on cylinders of ice of three different grain-size ranges, at temperatures $105 \leq T \leq 230$ K, imposed bulk shortening (engineering strain) rates $5 \times 10^{-5} \leq \dot{\varepsilon} \leq 7 \times 10^{-3} s^{-1}$ and confining pressures $0.1 \leq P \leq 300$ MPa, with most experiments run at 180 K and 50 MPa. The dependent variable measured was the differential stress σ required to maintain the imposed strain rate. Four of the samples were hydrostatically transformed to ice II before testing; the rest were ice I. Experimental conditions and summary results for all tests are listed in Tables 1–3, in which experiments are grouped according to phase and failure mode: ice I, ductile (Table 1, 15 runs, plus two samples given a ductile “prestrain”); ice I, Coulombic and plastic faulting (Table 2, 34 runs); and ice II, plastic faulting (Table 3, 4 runs). Additionally, we include here as Table 4 the results of an investigation of plastic

Table 2
Summary of Brittle Runs (Coulombic and Plastic Faulting), Ice I

Run	<i>d</i> (mm)	<i>T</i> (K)	<i>P</i> (MPa)	$\dot{\varepsilon}$ (s^{-1}) ^a	σ_{ult} (MPa)	Fault angle (°) ^b	Fault trace ^c	Hyperlink to		
								Photo	Chart	Log
671	0.25	105	50	7.4×10^{-5}	154.9	46	x, e	671p	671c	671b
679	0.68	195	25	5.6×10^{-4}	86.6	40	s, e	679p	n/a	679b
680	0.68	190	27	6.3×10^{-4}	95.2	45	s	680p	n/a	680b
688	0.68	210	20	5.7×10^{-3}	76.6	41	x	688p	688c(poor)	688b
689	0.25	175	20	5.7×10^{-3}	98.8	43	x, e	689p	689c(poor)	689b
690	0.68	175	20	6.5×10^{-3}	95.8	42	x, e	690p	690c(poor)	690b
692	0.25	180	40	5.8×10^{-3}	97.0	45	s	692p	692c	692b
695	0.68	180	50	5.8×10^{-4}	101.3	44	s, e	695p	695c	695b
696	0.68	180	10	5.7×10^{-4}	89.3	41	x, e	696p	696c	696b
697	0.68	180	20	5.7×10^{-4}	95.2	45	s, e	697p	697c	697b
698	0.68	180	3	5.7×10^{-4}	78.1	<25	x, e	698p	698c	698b
700	0.68	180	100	6.9×10^{-3}	106.7	43	x, e	700p	700c(poor)	700b
701	0.68	180	40	5.8×10^{-3}	95.8	45	s	701p	701c(poor)	701b
702	0.68	180	30	6.5×10^{-4}	108.8	46/44	s	702p	702c	702b
705	0.68	180	100	1.1×10^{-3}	108.1	45	m	705p	705c	705b
					87.8					
					129.3					
707	0.68	180	50	6.6×10^{-3}	100.0	43	m?, e	707p	707c(poor)	707b
708	0.68	180	0.1	2.9×10^{-3}	50.0	0	x	708p	708c	708b
709	0.68	180	150	3.5×10^{-3}	110.4 ^d	47	m	709p	709c(poor)	709b
					48					
713	0.68	180	50	4.0×10^{-4}	106.1	44	s	713p	713c	713b
714	0.68	180	100	8.4×10^{-4}	102.5	48	s, e	714p	714c	714b
715	0.68	180	50	3.0×10^{-4}	102.5	46	s	715p	715c	715b
717	0.25	180	50	9.5×10^{-4}	114.0	45	s	717p	717c	717b
718	0.25	180	50	8.0×10^{-4}	115.3	46	s, e	718p	718c	718b
724	1.18	180	50	3.0×10^{-4}	95.2	43	m?	724p	724c	724b
					64.7					
726	1.18	180	50	2.0×10^{-4}	88.8	43	s	726p	726c	726b
					87.8					
					129.3					
					87.8					
728	0.68	180	150	2.0×10^{-3}	111.0	46	m, e	728p	728c	728b
					93.9					
730	0.68	195	50	2.9×10^{-3}	95.2	45	x	730p	730c	730b
735	0.68	180	50	6.2×10^{-4}	90.9	47	s	735p	735c	735b
736	0.68	195	75	3.9×10^{-3}	96.4	46	s, e	736p	736c	736b
739(1)	0.68	180	50	1.0×10^{-4}	93.4	-	-	Ductile prestrain 0.045 (Table 1)		
739(2)	0.68	180	50	2.6×10^{-3}	102.5	46	s, e	739p	739p	739p
740(1)	0.68	180	50	1.3×10^{-4}	95.2	-	-	Ductile prestrain 0.065 (Table 1)		
740(2)	0.68	180	50	3.4×10^{-3}	98.0	43	s	740p	740c	740b
741(1)	0.68	180	50	6.1×10^{-4}	91.5 ^e	-	-	Ductile prestrain 0.0041		
741(2)	0.68	180	50	6.1×10^{-4}	104.3	45	s	741p	741c	741b
742(1)	0.68	180	50	5.9×10^{-4}	96.4 ^e	-	-	Ductile prestrain 0.0032		
742(2)	0.68	180	50	5.9×10^{-4}	104.9	46	x	742p	742c	742b
786	0.68	113	100	1.5×10^{-3}	142.7	46	s	786p	786c	786b

^aCalculated as bulk shortening rate. ^bWith respect to vertical. ^ce = touches or intersects end cap, m = multiple 45° faults, s = single fault, x = complex.

^dForce gage zero lost after first event. ^eMaximum σ ; piston stopped before failure.

faulting performed nearly three decades ago, whose σ_{ult} values are published in Kirby et al. (1991) but whose chart recordings and sample photographs have otherwise gone unanalyzed. Those experiments emphasized generally lower T and higher P and are a useful complement to the more recent experiments. Full data sets for the runs in Tables 1 through 4, including some ancillary materials such as micrographs, are viewable through links in the tables. Comparative load-displacement chart records for the runs in Tables 2 and 4 (excepting those with legibility problems) are provided in Figure S2.

Table 3
Summary of Runs, Ice II (All Plastic Faulting)

Run	d (mm)	T (K)	P (MPa)	$\dot{\varepsilon}$ (s^{-1}) ^a	σ_{ult} (MPa)	Fault angle ($^{\circ}$)	Hyperlink to		
							Photo	Chart	Log
737(1)	0.05	110	150	1.9×10^{-4}	221.6 ^b	-	737p	737c	737b
737(2)	0.05	110	100	4.7×10^{-4}	207.7 ^b	-	737p	737c	737b
737(3)	0.05	110	100	4.7×10^{-3}	205.0 ^b	-	737p	737c	737b
737(4)	0.05	110	50	9.4×10^{-4}	194.0 ^{b, c}	46	737p	737c	737b
743	0.05	112	150	4.7×10^{-3}	153.9 ^d	44	743p	743c	743b
746	0.05	105	150	1.8×10^{-4}	288.6	45	746p	746c	746b
781	0.05	105	250	1.8×10^{-4}	275.2	49	781p	781c	781b

^aCalculated as bulk shortening rate. ^bStop before ultimate failure. ^cSample faulted 10 s after stop. ^dChart record shows four unusual stress drops before σ_{ult} ; suspect jacket leak.

The initial response to loading at constant displacement rate is elastic, with σ and ε increasing linearly with time (e.g., Figure S2). Linear slopes correspond to a column modulus of ~5 GPa per unit strain in the sample but include an elastic contribution from steel column parts (far stiffer but far longer, Figure S1) so is reasonably consistent with the modulus of 9 GPa for polycrystalline ice measured at megahertz frequencies (Gammon et al., 1983; Vaughan et al., 2016). Linearity ceases at the yield point, the first appearance of inelasticity. Yielding and achievement of σ_{ult} are almost simultaneous in brittle failure, and the event is catastrophic and audible, often jolting the entire apparatus. It is typically accompanied by an immediate stress drop of 75% or more from σ_{ult} and a corresponding jump in sample shortening. Under most conditions in these experiments, the fault plane is inclined at approximately 45° to the stress axis (Figures 1a and 1b), consistent with plastic faulting. Where the indium jacket remains intact following the failure event, effective confinement is maintained, and the cycle of elastic loading and faulting can repeat as the loading piston continues inward at the prescribed rate. Virtually all faulting events in this work at $P > 20\text{--}30$ MPa maintain the qualitative character of plastic faulting, covering a wide range of temperatures (105–210 K) and strain rates ($\dot{\varepsilon} = 7 \times 10^{-5} - 7 \times 10^{-3} s^{-1}$) and including ice II as well (Figure 1b). In the case of ductile failure, the transition from first yield to the achievement of peak stress σ_{ult} and beyond is generally smooth and without sudden change. For previously undeformed polycrystalline ice, strength decreases over a few percent

Table 4
Summary of Earlier Runs, Ice I (All Plastic Faulting)

Run	d (mm)	T (K)	P (MPa)	$\dot{\varepsilon}$ (s^{-1}) ^a	σ_{ult} (MPa)	Fault angle ($^{\circ}$) ^b	Fault trace ^c	Hyperlink to		
								Photo	Chart	Log
261	0.68	77	200	3.4×10^{-4}	162.1	50	x	261p	261c	261b
262	0.68	77	200	3.4×10^{-4}	155.2	52	s	262p	262c	262b
263	0.68	77	100	3.4×10^{-4}	164.2	44	s	263p	263c	263b
265	0.68	77	100	3.4×10^{-4}	160.0	39	x	265p	265c	265b
					116.6					
					110.1					
					97.6					
269	0.68	77	300	3.3×10^{-4}	160.5	~45	s	269p	269c	269b
270	0.68	119	200	3.3×10^{-4}	141.4	~45	m	270p	270c	270b
					133.6					
271	0.68	118	100	3.3×10^{-4}	140.2	~45	x	271p	271c	271b
					121.4					
					120.1					
272	0.68	171	200	3.3×10^{-4}	106.3	48/49	x	272p	272c	272b
273	0.68	172	100	3.3×10^{-4}	106.9	46	s	273p	273c	273b
308	0.68	159	200	3.3×10^{-4}	120.5	48	s	308p	308c	308b
309	0.68	160	300	3.3×10^{-4}	111.5	46	s	309p	309c	309b

Note. T, P, and σ_{ult} values published previously (Kirby et al., 1991).

^aCalculated as bulk shortening rate. ^bWith respect to vertical. ^cm = multiple 45° faults, s = single fault, x = complex.

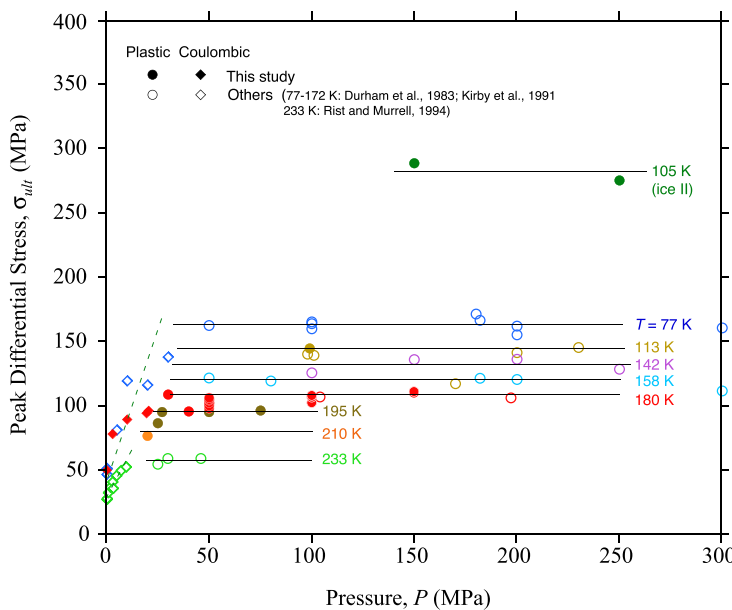


Figure 2. Peak differential stress (=ultimate strength σ_{ult}) versus confining pressure for brittle failure of ice I and ice II at $T = 77\text{--}233\text{ K}$. Points in this study from Table 2 (ice I) are restricted to those of grain size 0.68 mm. Temperatures are indicated by color, as labeled. Horizontal lines indicate average strength in plastic faulting (solid symbols) at each temperature. Dashed lines are best-fit linear regressions to the observed pressure-dependent failure strength in Coulombic faulting (open symbols) at 77 and 233 K. Points from Table 4 are plotted with “others” since the σ_{ult} values themselves have already been published. Data for the first two ice II runs (Table 3) are not plotted.

strain to a near steady-state level (σ_{ss} in Table 1) typically 10–20% below σ_{ult} . Spatial distribution of strain across the sample is broadly uniform, although intriguing jacket rumpling at the few millimeter scale (Figure 1c) hints at local heterogeneities in strain rate.

3.1. Plastic Faulting

In Figure 2, values of ultimate strength σ_{ult} for faulting experiments in this study (Table 2) and those published by others are plotted as a function of P for a range of T values. Our concentration here at 180 K (solid red figures) is apparent. The domain of plastic faulting exists above $P \approx 30\text{ MPa}$, where the isotherms are horizontal (i.e., P independent) and shear fault inclinations are approximately 45°. Actual fault inclinations for the 34 faulted ice I samples tested here at $P \geq 30\text{ MPa}$ are $45.4^\circ \pm 2.3^\circ$ (1 SD) (Table 2), as derived from photographs (e.g., Figure 1a) and polished sections, which were made of several samples in the sequence of runs 688–702. The latter can be viewed by following hyperlinks in the first column of Table 2. In the three lowest pressure runs ($P \leq 10\text{ MPa}$), σ_{ult} is strongly P dependent, and fault planes are irregular and generally steeply inclined (Figure 1d), consistent with Coulombic faulting. The nature of the transition from Coulombic to plastic faulting at 10–30 MPa at 180 K is addressed in more detail in section 3.4. It is worth noting that the scatter in values of σ_{ult} in the plastic faulting regime is 10% or less. There are too few data for ice in the Coulombic regime for comparison, but for crustal rocks, scatter in σ_{ult} in the Coulombic regime is considerably more than 10% (Byerlee, 1967; Lockner, 1995; Lockner et al., 1982).

A monotonic increase in σ_{ult} with decreasing temperature is evident in Figure 2. Plotting the mean σ_{ult} (P) values against T (Figure 3) shows that the temperature trend is approximately linear, suggesting commonality to the mechanism of plastic faulting over a broad range of temperatures. Being linear in T , such a common mechanism, should it exist, would probably not derive its T dependence from Arrhenius-type thermal activation. We note that the data do support a model of two or three different thermally activated processes at different intervals along the T axis (Figure 3 inset). Also, regarding T dependence, overlaid in Figure 3 is the flow law for polycrystalline ice I in the steady-state ductile regime at typical laboratory strain rates illustrating why, when studying the transition from plastic faulting to ductile flow in the lab, the accessible temperature range centered at ~180 K is decidedly narrow.

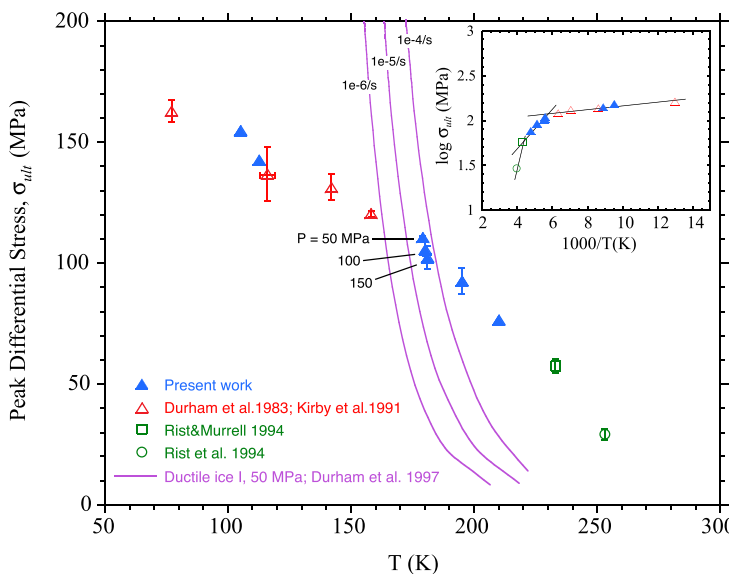


Figure 3. Failure strength of ice in plastic faulting versus temperature from several different studies, showing a continuous trend from 77 K to near the melting point. Points shown with error bars are the mean and standard deviation of a group of measurements at the same temperature and pressure. Grain size, pressure, and strain rate vary among points. The three labeled triangles at 180 K (shifted slightly in T for plotting purposes) are grouped by pressure. Steady-state ductile flow of ice in the grain-size-insensitive regime at three different strain rates is superposed in purple. Inset: the same data presented as an Arrhenius plot. Straight lines have slopes proportional to $\exp(-A/T)$, where A is a constant, as would happen were points generated by a thermally activated process (in which case $A = E/R$, where R is the gas constant and E is an activation energy).

3.2. Multiple Events

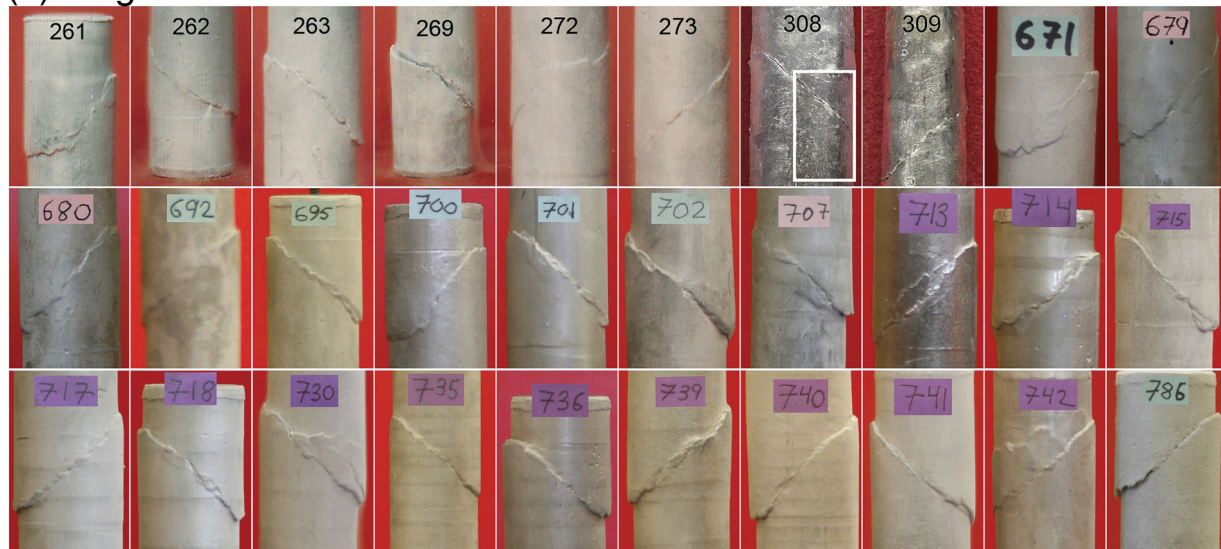
Of the 38 plastically faulted samples in Tables 2 and 4 (27 runs for which $P > 20$ MPa, that is, those that plastically faulted according to Figure 2) and (11 runs), integrity of the indium jacket was apparently maintained after initial brittle failure in eight of the runs, and subsequent cycles of loading and brittle failure were recorded. Severe jarring of the apparatus, as sometimes occurs, can mechanically displace the zero setting of the force gage transducer, thus degrading stress resolution following the first event. However, despite the loss of resolution, the appearance of load-displacement curves for subsequent events is at least consistent with a significant, if not complete, recovery of sample strength. Good examples are records of the four multiple-event runs in Figure S2 (705, 724, 726, and 728), where shapes of load-displacement curves for subsequent events generally parallel those of the first events in their linear slope, slight curvature, and sudden dropoff, although sometimes with considerable vertical offset (up or down).

Examination of fault traces on the indium jackets from these samples suggests that multiple failure events and multiple 45° fault traces are correlated (Figure 4). The fault traces are usually parallel and close together, although for run 709, the faults are conjugate but not intersecting. Of the eight multiple-event runs (Figure 4b), three (265, 271, and 726) show no clear sign of multiple fault traces, although in two of those (265 and 271), the tendency for multiple fault formation may have been mitigated by the intersection of fault and steel end cap. A plastic fault thus remains cohesive, a sign that fault displacement is the result of plastic rather than crack-related deformation as in Coulombic faulting. For run 709, with planes in conjugate orientations that do not intersect, the conclusion is compelling: It is difficult to envision how two faults so far apart (~5 mm at closest approach) could have initiated simultaneously. Multiple fault planes and fault bifurcations do occur in some single-event runs, but the proportion of such samples is small.

3.3. Prestrain Experiments

Four runs in Table 2, numbered 739–742, were “prestrain” experiments at fixed $P = 50$ MPa and $T = 180$ K, wherein we imposed a ductile strain step prior to the plastic faulting step as a probe of possible microstructural origins for the phenomenon. Ductile prestrains of neither $\varepsilon \approx 0.05$ at low strain rate to 80% of expected

(a) Single event



(b) Multiple events



Figure 4. Photographs of fault traces expressed on indium jackets for all samples in Tables 2 and 4 for which $P > 20$ MPa, separated into two groups according to whether the run had (a) a single faulting event or (b) multiple events with strength recovery. Run numbers labeled. Note the apparent correlation of multiple events with multiple faults. Jacket photos of runs 308 and 309 were taken after removal of the sample from inside. A portion of the inner surface of jacket 308 (white outlined box) is enlarged in Figure 11a.

faulting strength nor $\varepsilon \approx 0.004$ at 90% had a detectable effect on the peak stress at plastic faulting. The value of peak stress for the four prestrained samples is all in the range of 105 ± 5 MPa, which compares well to the value $\sigma_{\text{ult}} = 106.8 \pm 4.8$ MPa of six nonprestrained brittle runs at similar conditions. Thus, we cannot detect any effect on plastic faulting of processes that occur at low strain, processes that are likely to include a substantial increase in dislocation density, partial recrystallization, and phase change. The related matter of an unavoidable inelastic strain before faulting is discussed in more detail in section 3.5 below.

3.4. Crossover From Plastic Faulting to Ductile Flow

In rocks, where brittle behavior is typically Coulombic, the so-called brittle-to-ductile (B-D) transition typically extends over many tens of MPa in pressure, as pressure-insensitive ductile processes account for an increasing proportion of imposed strain with increasing confining pressure (Byerlee, 1968; Evans et al., 1990; Kohlstedt et al., 1995). In this respect ice is very unrock like: Apart from the precursor phenomenon discussed in the next section, the B-D transition in ice with changing pressure, where the brittle process is plastic faulting rather than Coulombic, is vanishingly narrow within resolution limits (Figure 2). The maximum widths of the B-D transition allowed by the data as plotted on axes of σ_{ult} versus $\dot{\varepsilon}$ for several grain sizes (Figure 5) and pressures (Figure 6) are shown as colored parallelograms for runs at 180 K. Also, plotted as dashed lines in Figures 5 and 6 are the trends for peak stress, σ_{ult} , in the ductile field, which follows a power-law relationship $\sigma_{\text{ult}} = \dot{\varepsilon}^{1/n}$ where $n \approx 6$ on the basis of our sparse data set. This is a somewhat higher value than the $n = 4$ value for steady-state dislocation creep (e.g., Durham et al., 1997). Similar to the steady state, however, there is no dependence on grain size (Figure 5) at these grain sizes, and there is a negative dependence of strength upon pressure (Figure 6) (Durham et al., 1983).

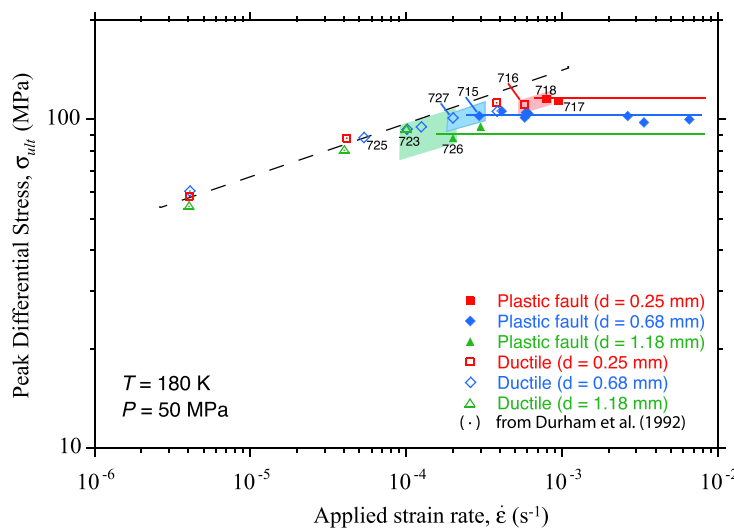


Figure 5. Plastic faulting-to-ductile (B-D) transition for three different grain sizes (coded by color and symbol shape) at fixed conditions of pressure and temperature as labeled. Dashed line is an estimated fit to the peak stresses of the six ductile runs (open symbols) of strain rate $<10^{-4} s^{-1}$. The slope of the dashed line is approximately $1/6$ ($n = 6$), significantly less than the $n = 4$ value applicable to steady-state flow. Horizontal lines indicate average strength of plastic faulting (solid symbols) by grain size. Shaded parallelograms enclose the three pairs of runs constraining the width of the B-D transition at each of three different grain sizes. Chart records for the three pairs of runs (run numbers are labeled) constitute the top row of Figure 7.

The sample-to-sample precision in location of the B-D transition across all experiments is striking: The width of the colored parallelograms indicates that the transition is constrained to lie within a range of a factor of ≤ 2 in strain rate. For $n = 6$, that width is roughly the equivalent of a $\pm 10\%$ scatter in σ_{ult} (Figure 2). The minimum widths cannot be distinguished from a point-like crossover. Furthermore, among the roughly 16 ductile and brittle data points concentrated near the transition at each condition, only one is on the “wrong” side of the transition, that of a ductile run in the brittle field at 50 MPa and $d = 0.68$ mm (thus visible in both Figures 5 and 6).

Grain-size dependence of strength (Figure 5) is largely absent in the ductile field, consistent with the high n value, but is distinct in the brittle field, with σ_{ult} increasing with decreasing grain size. The B-D crossover thus shifts to higher stress and higher strain rate with decreasing grain size roughly following the $n = 6$ ductile flow law. The behavior can be rationalized in terms of grain size effects in either the ductile or brittle fields. A small amount of grain-size-sensitive ductile deformation at lower grain size, too little to deflect the dashed line in Figure 5, could be sufficient to relieve high local stresses that might otherwise trigger brittle instability. Alternately, if flaw size in the brittle field is related to grain size, the finer-grain material should require higher stress to reach criticality, in the manner of classic materials toughening by crack blunting (Schulson, 1990).

By contrast, the pronounced influence of pressure on the location of the B-D crossover (Figure 6), an increase by nearly an order of magnitude in strain rate as P increases from 50 to 150 MPa, is well in excess of the well-known P -dependent weakening in the ductile field (Durham et al., 1983). The strain-rate enhancement is, however, easily explained by a small amount of bulk (i.e., distributed) phase transformation of ice I to ice II, which can occur at conditions near those of these tests (Durham et al., 1983). As an example, bulk transformation is manifest in the load-time curves of the two highest-pressure ice I runs here: 706 and 710 (Table 1). Details are provided in Figure S3. Since conditions in the brittle and ductile fields are essentially indistinguishable at the B-D crossover, we must therefore consider the possibility that brittle failure near the crossover is also preceded by some amount of phase transformation.

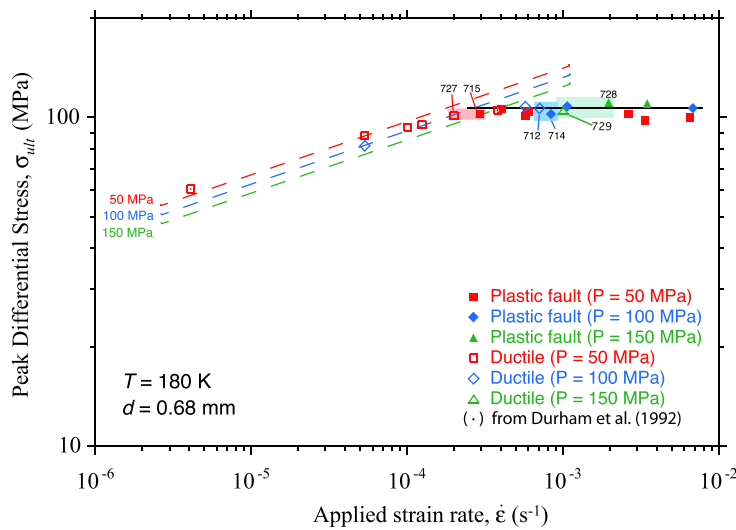


Figure 6. Plastic faulting-to-ductile (B-D) transition for three different pressures (coded by color and symbol shape) at fixed conditions of grain size and temperature as labeled. Dashed lines are taken from Figure 5 with vertical positions offset to account for pressure on the basis of $-13 \text{ cm}^3/\text{mol}$, the activation volume for steady-state creep of ice at these conditions (Durham et al., 1997). Shaded rectangles enclose the three pairs of runs straddling the B-D transition at each of three different pressures. Chart records for the three pairs of runs (run numbers are labeled) constitute the bottom row of Figure 7. The data points at 50 MPa, red squares (open and closed), also appear in Figure 5 as blue diamonds.

3.5. Inelastic Precursors and Phase Transformation

Consistent with the strain-rate enhancement apparent in Figure 6, among all the available chart records for the runs in Tables 2 and 4 (Figure S2), many of the load versus time traces show a slight curvature away from elastic linearity in the moments leading up to brittle failure. The same is true by definition for the ductile runs (Table 1). Remarkably, the two sets of precursors, those preceding ultimate failure by brittle and by ductile mechanisms, are difficult to distinguish. Figure 7 shows side-by-side comparisons of prefailure load-time records for the five pairs of runs that most tightly constrain the B-D crossover locations in Figures 5 and 6, where test conditions are identical except for the slight difference in strain rate (the pair 715–727, $d = 0.68 \text{ mm}$, $P = 50 \text{ MPa}$ appear in both figures). Prefailure, apart from subtle differences in imposed displacement rate, there is little in the way of distinguishing features of the load-time curves and little upon which to anticipate whether the ensuing failure would be violent or controlled.

It is improbable that brittle and ductile failure mechanisms produce essentially identical load-time records prior to ultimate failure, even versus changes in grain size and pressure. If the precursive mechanisms are the same and prefailure strain in ductile samples includes some amount of bulk phase transformation, as suggested two paragraphs above, then the inelastic precursor to brittle failure must also include some phase transformation. That conclusion is singularly impactful, given the widely hypothesized role of phase transformation in plastic faulting in geologic materials. It would therefore be useful to determine whether bulk phase transformation in our experiments plays a causal role in plastic faulting or if it is entirely passive. Other than Figure 7, which suggests the latter, are there any characteristics or dependencies of precursive phase transformation that might suggest a link to plastic faulting?

It is possible to estimate the proportions of ordinary plastic strain, $\varepsilon_{\text{creep}}$, and strain due to phase transformation, $\varepsilon_{\text{I} \rightarrow \text{II}}$, in the inelastic precursors. Total precursive strain, ε_{tot} , is calculable from the load-time record, starting sample length, and piston displacement rate. We can also estimate $\varepsilon_{\text{creep}}$ based on the flow law for steady-state, grain-size-independent creep of ice I under essentially identical laboratory circumstances and test conditions (Durham et al., 1997), which surely underestimates the strength (and overestimates strain rate) in ice that has not yet yielded (were undeformed ice weaker than ice in the steady state, it would by definition be impossible to achieve any stress above steady-state level). The difference, $\varepsilon_{\text{tot}} - \varepsilon_{\text{creep}}$, should be a conservative (i.e., under-) estimate of transformational strain, $\varepsilon_{\text{I} \rightarrow \text{II}}$ in the precursor.

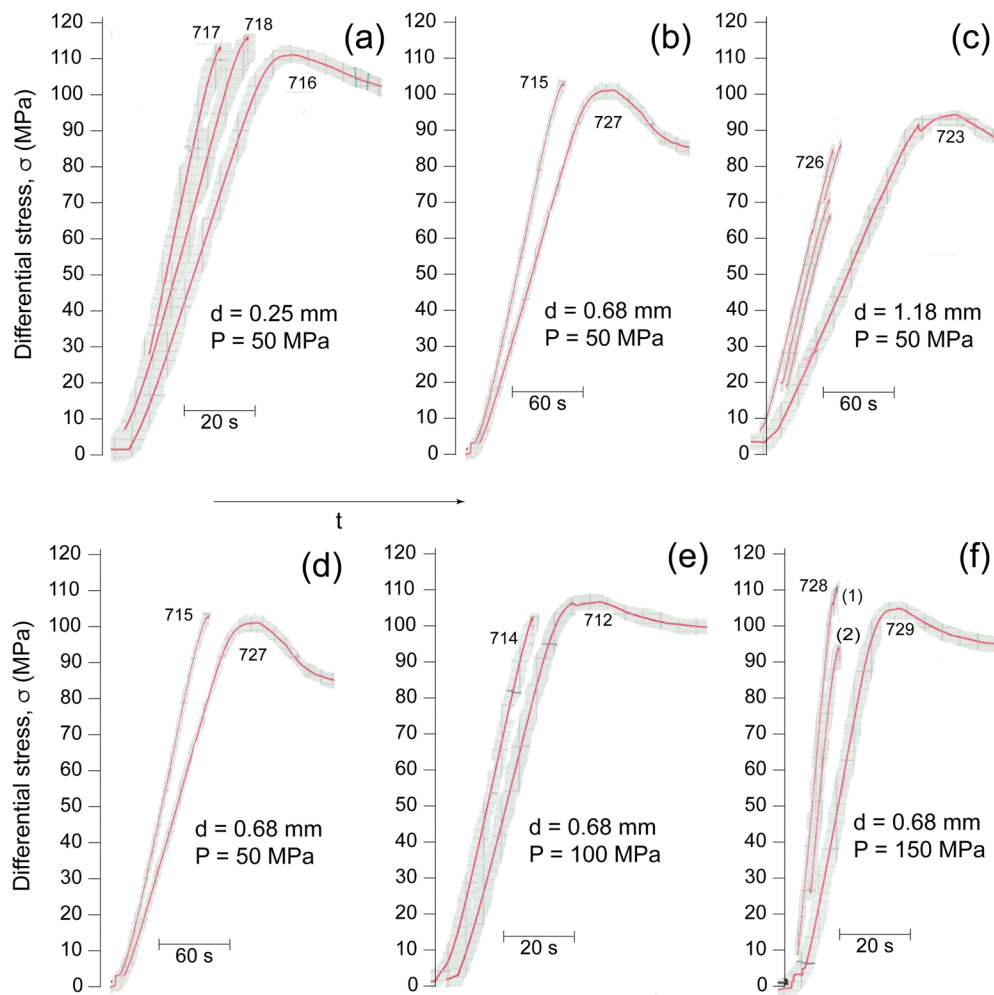


Figure 7. Differential stress versus time chart traces for pairs of brittle and ductile runs most tightly straddling the B-D crossover at 180 K, the members of each pair differing only in applied strain rate, for five different sets of grain size and pressure conditions (panel (a) has an additional brittle run; panels (b) and (d) are identical). Brittle runs are those whose trace terminates abruptly during loading; ductile runs are those whose strength rises to its ultimate level and then drops smoothly to a nonzero steady-state level. Traces for all five ductile runs continue to the right and are truncated here for presentational purposes. Note that curved portions of records prior to failure for brittle versus ductile are difficult to distinguish in any given panel. Among the ductile curves, there are a number of small “blips” (runs 723 and 712) or breaks in slope (712, 723, 727, and 729), which may be hints of incipient plastic faulting that failed to propagate. In brittle run 728 a subtle blip can be seen just prior to failure. Top row (a-c) grain-size dependence, corresponding to Figure 5; bottom row (d-f) pressure dependence, corresponding to Figure 6. For multiple brittle events (c and f), the absolute vertical position of the curve is known only for the first event.

Results of the calculation are tabulated in Tables 5 and 6 (a more detailed description of the calculation is provided in Text S1; all three tables [Tables 5, 6, and S1] include links to graphical calculations). The magnitudes of precursive strain are generally very low, with only eight of 29 runs exhibiting $\varepsilon_{\text{tot}} > 0.002$. Because the durations of the precursors are typically short in time (Table S1), values of $\varepsilon_{\text{creep}}$ tend to be small, leaving $\varepsilon_{\text{I} \rightarrow \text{II}}$ to predominate. It is also important to note that because of the large volume decrease associated with ice I \rightarrow II and because the contraction under nonhydrostatic stress is highly anisotropic, being accommodated almost entirely by shortening in the direction of maximum stress (Kirby et al., 1991), the extent of implied bulk phase transformation in Table 5 is subtle. Most values of $\varepsilon_{\text{I} \rightarrow \text{II}}$ in Table 5 require <1% of the ice I in a sample to transform to ice II. Dependence of $\varepsilon_{\text{I} \rightarrow \text{II}}$ on environmental variables is illustrated in Figure S4. Systematics are elusive given the sparse sampling. The clearest signal is a positive dependence of $\varepsilon_{\text{I} \rightarrow \text{II}}$ on confining pressure P above 100 MPa (Text S2 and Figure S4a).

Table 5
Ductile Precursors in Table 2^a

Run ^a	d (mm)	T (K)	P (MPa)	σ_{ult} (MPa)	$\varepsilon_{\text{tot}} \times$ 1,000	$\varepsilon_{\text{creep}} \times$ 1,000	$\varepsilon_{\text{I} \rightarrow \text{II}} \times$ 1,000
671	0.25	105	50	154.9	0.30	2.5×10^{-12}	0.30
692	0.25	180	40	97.0	0.00	0.01	
695	0.68	180	50	101.3	0.43	0.12	0.31
696	0.68	180	10	95.2	0.00	0.05	
697	0.68	180	20	78.1	0.17	0.08	0.09
698	0.68	180	3	89.3	0.00	0.02	0.00
702	0.68	180	30	108.8	0.97	0.19	0.78
705	0.68	180	100	108.1	0.75	0.21	0.54
	0.68			87.8	2.14	0.10	2.04
	0.68			129.3	1.50	0.53	0.96
708	0.68	180	0.1	50.0	0.00	0.00	
713	0.68	180	50	106.1	1.37	0.38	0.99
714	0.68	180	100	102.5	1.09	0.21	0.88
715	0.68	180	50	102.5	1.65	0.52	1.14
717	0.25	180	50	114.0	1.71	0.26	1.45
718	0.25	180	50	115.3	1.91	0.37	1.54
724	1.18	180	50	95.2	0.48	0.21	0.27
	1.18	180	50	64.7	0.45	0.03	0.42
726	1.18	180	50	83.0	0.20	0.16	0.04
	1.18			87.8	0.80	0.28	0.53
	1.18			129.3	0.82	0.09	0.73
	1.18			87.8	0.64	0.07	0.57
728	0.68	180	150	111.0	3.55	0.63	2.92
	0.68			93.9	6.51	0.28	6.23
730	0.68	195	50	95.2	0.88	0.58	0.30
735 pre ^b	0.68	180	50	89.1	0.16	0.07	0.09
735	0.68	180	50	90.9	0.00	0.03	
736	0.68	195	75	96.4	3.15	1.09	2.07
739	0.68	180	50	107.4	0.63	0.04	0.59
740	0.68	180	50	98.0	0.63	0.03	0.60
741	0.68	180	50	104.3	1.10	0.23	0.87
742	0.68	180	50	104.9	2.47	0.35	2.12
786 pre ^b	0.68	113	100	135.4	0.45	2.0×10^{-11}	0.45
786	0.68	113	100	142.7	0.00	1.3×10^{-11}	

^aExcluding nine runs with entries in “chart” column of Table 1b labeled “(poor)” or “n/a.” ^bPrecursive “blip” occurred before ultimate failure.

samples with the highest amounts of $\varepsilon_{\text{I} \rightarrow \text{II}}$ (272, 273, 309, and 728, locations labeled in Figure 8), three failed actually at the kinetic limit. We suspect that this is a manifestation of stress concentrations in a limited volume (<1%) of material. Local stresses far in excess of applied stress have been observed by SEM-EBSD near grain boundaries in deformed copper (Jiang et al., 2013), marble (Mariani et al., 2018), and olivine (Wallis et al., 2019). A similar argument relating local stress concentrations to plastic faulting is deferred to section 4 below.

3.7. Plastic Faulting in Ice II

Figure 2 also includes the first observations of plastic faulting in ice II, in two experiments at 105–110 K, not otherwise invalidated by circumstances of testing (Table 3). Fault inclinations are near 45° (Table 3, Figure 1b), and σ_{ult} levels are consistent with no P dependence, being nearly indistinguishable despite a difference in P of 100 MPa. Plastic faulting has been identified in only a limited number of rock types, so it is intriguing that two polymorphic crystalline phases of the same component are on that short list. Mapped onto Figure 8, the conditions for plastic faulting in ice II lie 100–200 MPa below a dashed line extension of the ice II/VI equilibrium phase boundary. Given the II → VI volume reduction of ~12%, there may be a first impression of parallel behaviors in plastic faulting in ice I and ice II. However, not only is the comparison with respect to a kinetic limit for ice I and an equilibrium boundary for ice II, but also as with I → II, the II → VI transformation is also kinetically inhibited and to a far

3.6. Maximum Normal Stress

To return to the question of a causal or passive role of bulk phase transformation in the context of plastic faulting, in Figure 8, we map the two phenomena on the equilibrium phase diagram for ice. As indicated in section 1, ice I → II is kinetically inhibited, as are most of the reconstructive phase transformations in ice (Bridgman, 1912), requiring a T -dependent overpressure to proceed on the laboratory time scale. As observed in our experiments, the kinetic limit, that is, the overpressure boundary of the kinetically inhibited zone, is defined by the red crosses in Figure 8 for the case of hydrostatic pressurization. As can be seen in Figure 8, the overpressure required at 180 K for the I → II transformation exceeds 100 MPa. Nonhydrostatic stress often assists phase transformation (Wheeler, 2014), and ice I → II is no exception: We have observed that the kinetic limit under nonhydrostatic stress is better correlated to the maximum normal stress ($\sigma_1 = \sigma + P$) (blue dots in Figure 8) than to either P or mean stress $(\sigma_1 + 2P)/3$ (Kirby et al., 1991). Using a maximum normal stress axis in Figure 8 thus allows us to compare directly the kinetic limit for bulk transformation under nonhydrostatic stress to the conditions for plastic faulting from Figure 2.

Looking at the range of conditions under which plastic faulting occurred, along the broad horizontal lines in Figure 8, one difficulty with a link to phase transformation becomes apparent: Most occurrences of plastic faulting fall well short of the I → II kinetic limit, many by >100 MPa. Moreover, the broad spread of σ_1 values over which faulting occurs at any temperature means that the variable that exerts primary control over bulk phase transformation, namely, σ_1 , has little control over plastic faulting.

Although we have equated precursive bulk transformation, $\varepsilon_{\text{I} \rightarrow \text{II}}$, to macroscopic bulk transformation in the sense that both are nonlocalized phenomena, recall that while macroscopic bulk transformation occurs at the kinetic limit in Figure 8, finite precursive $\varepsilon_{\text{I} \rightarrow \text{II}}$ was inferred at virtually every location in this study where plastic faulting occurred (Tables 5 and 6), and many of those locations are distant from the kinetic limit, as just discussed. Note also that of the four plastically faulted sam-

Table 6
Ductile Precursors in Table 4

Run	<i>d</i> (mm)	<i>T</i> (K)	<i>P</i> (MPa)	σ_{ult} (MPa)	$\varepsilon_{tot} \times$ 1,000	$\varepsilon_{creep} \times$ 1,000	$\varepsilon_{I \rightarrow II} \times$ 1,000
261	0.68	77	200	162.1			
262	0.68	77	200	155.2			
263	0.68	77	100	164.2			
265	0.68	77	100	160.0			
				116.6			
				110.1			
				97.6			
269	0.68	77	300	160.5			
270	0.68	119	200	141.4			
				133.6			
271	0.68	118	100	140.2			
				121.4			
				120.1			
272	0.68	171	200	106.3	8.65	0.77	7.88
273	0.68	172	100	106.9	6.26	0.27	5.98
308	0.68	159.3	200	120.5	0.16	0.01	0.15
309	0.68	159.8	300	111.5	2.30	0.05	2.25

Note. For runs 261–271, at $T \leq 119$ K, no precursor was observed, that is, $t_{lag} = 0$.

greater degree than that of ice I \rightarrow II (Mishima & Endo, 1980). In fact, the kinetics of II \rightarrow VI are so slow that identification of the location of the II/VI equilibrium univariant below 200 K (near 600 MPa) is technically infeasible. The kinetic limit below 200 K is observed to extend rapidly toward higher pressure, reaching >1 GPa at 170 K, the lowest T to which it has been observed (Mishima & Endo, 1980). If there is phase transformation involving the ice II samples at 110 K, the equilibrium phase diagram is of little help determining what the daughter phase might be.

3.8. Microstructural Imaging

Sections through three of the plastically faulted samples were also examined by EBSD using a Zeiss SIGMAVP field emission scanning electron microscope following procedures outlined in Prior et al. (2015). All specimens were stored at $T = 77$ K between loading and imaging but were warmed to 220 K for periods of several minutes during preparation and mounting (Prior et al., 2015).

All three faults imaged (Figure 9) show bands of finer grains that define the fault trace. In run 671 (Figure 9a) the thickness of the zone of finer grains is highly variable. The fault in run 724 (Figure 9b), presumably related to one of its multiple failure events, shows a width of $<0.05\text{--}0.2$ mm and an irregular trace with undulations larger than the width

of the fracture. From the morphology of the indium jacket, the total fault displacement in two events was ~ 1 mm (Figure 4). The fault in run 730 (Figure 9c) is better organized, with a fault width 0.3–0.5 mm and grain sizes within the fault of 1–10 μm . Displacement along the fault is roughly 2 mm (Figure 4). There is no sign of liquid formation, for example, fracture or embayment filling, in any of the images. There are many instances of narrow bands and pockets of fine-grained material off the main fracture (Figures 9b and 9c), but the bands are generally tortuous and very uncrack like, being more suggestive of recrystallization along grain boundaries. A particularly good example occurs in sample 730 (Figure 9c: top right inset). This is a conjugate band of fine grains. The band is from a location above and to the left of the main fault figure. Local irregular and lobate boundaries occur in all samples most commonly on the boundaries between the original large grains (e.g., run 730 big grains on the left side: Figure 9c) and more rarely on the margins of bands of small grains (e.g., run 671: Figure 9a inset). Often, the margins bordering small-grain areas contain small subgrains, with low-angle boundaries, and which are similar in size to the small grains. These are most clearly seen in boundary maps (e.g., Figure 9c top right inset). Large (original) grains are often distorted. Where the bands of small grains along faults are thick, there are sufficient small grains to define a crystallographic preferred orientation (CPO). CPOs from such zones in runs 671 and 730 have weak maxima of *c*-axes (i.e., [0001]) in a direction close to perpendicular to the fault trace (Figures 9a and 9c). There is considerable evidence of inherited orientations from original grains. In sample 724 narrow bands of small grains have CPOs where the maxima correspond to the larger grains from the same area (Figure 9b), but the small grain CPOs are much more dispersed. In Figure 9c a chain of red grains occurs inside the box outlined in yellow. These have very similar orientations to the large red grain below and left of the box and are interpreted as inherited from that grain.

The small grains are reasonably interpreted as recrystallized grains, and there is microstructural evidence outlined above that is consistent with the operation of deformation, recovery, and subgrain rotation recrystallization and also with strain-induced grain boundary migration. The weak CPOs are consistent with those generated in experimental shear of ice at low temperatures and/or fast rates (Qi et al., 2019) and interpreted by the same authors as being related to coupled operation of rotation due to dislocation motion, recrystallization, and grain boundary sliding. The dispersion of inherited orientations has been interpreted in terms of grain boundary sliding processes being more effective in fine recrystallized grains (Bestmann & Prior, 2003; Craw et al., 2018).

Microstructures can sometimes be complicated by overprinting effects of catastrophic postfailure energy release. We can attempt to reconcile the fault image in run 724 (Figure 9b) with the concept discussed

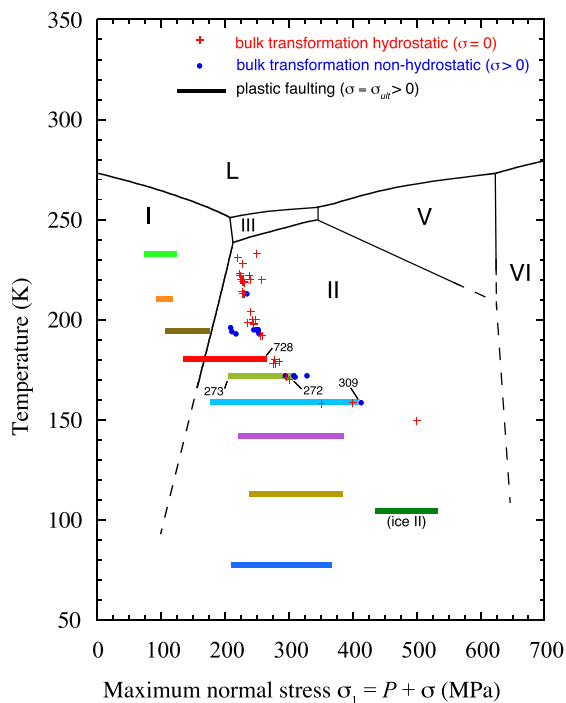


Figure 8. Experimental values of maximum normal stress ($\sigma + P$) for the ice I \rightarrow II bulk phase transformation under hydrostatic (red crosses) and non-hydrostatic loading (blue dots) at typical “lab” rates of a few to several MPa/s (Kirby et al., 1991). Ranges of $\sigma_{\text{ult}} + P$ values from Figure 2 for plastically faulted samples at each temperature are shown as horizontal bars. Coding of plastic faulting T by color matches the scheme in Figure 2. Background is the low P portion of the phase diagram of H_2O that includes the liquid (L) and five of the crystalline ice polymorphs (Roman numerals). Equilibrium boundaries of I/II and II/VI below ~ 170 K are difficult to establish because of slow reaction kinetics and are shown as dashed lines. The crosses and dots map the experimentally determined conditions required to overcome the kinetic limitation of the I \rightarrow II transformation. Noteworthy is the co-location of the nonhydrostatic and hydrostatic kinetic limit (Kirby et al., 1991). Plastic faulting does not occur beyond the kinetic boundary, and the fact that many faulting events (bars) occur at locations distant from the kinetic limit, many by >100 MPa, suggests that the plastic faulting mechanism is unrelated to the mechanism of bulk ice I \rightarrow II transformation. Run numbers label the test conditions for four runs discussed in section 3.6.

with numerous broad regions of positive topography, a clear signature of ice II. The quasi-rectilinear shape of the ice II domains, with edges aligned along the maximum shear direction, is perhaps not surprising since bulk transformation is enhanced by shear stress (Figure 8). The association of ice II regions with the fault in Figure 10 clearly suggests a causal relationship. Given the uniaxial symmetry of the state of stress before faulting, if the morphology of ice II inclusions is influenced by shear stress, one might expect to see prefaulting ice II formations aligned along 45° planes of various azimuth around the vertical direction. The fact that most ice II inclusions in Figure 10 are parallel to the same plane that in addition is that of the fault is strong evidence that faulting preceded ice II formation. Ice II regions bordering the fault must have formed after faulting, since matching clipped portions do not appear below the fault. On the other hand, run 273 showed an unusually large inelastic precursor (Table S2), meaning that there must have been extensive ice II formation before faulting.

The paradox is partly explained by the images of plastically faulted run 308 (Figure 11a, a1). Here, dense domains of much smaller point-like ice II inclusions are aligned in various orientations with respect to

above that GSS deformation of material within the faults is responsible for the high strain rates and large displacements of plastic faulting. In the first event in run 724, differential stress σ dropped from approximately 100 to 25 MPa (Figure S2), while the sample shortened axially by 1.0 mm, approximately half of the measured shortening of 1.8 mm. Thus, displacement along the fault was 1.4 mm, and total inelastic shear strain in the 0.3-mm-wide fault (Figure 9b) was ~ 5 . Assuming that stress drop versus displacement was linear, the work done on the sample was approximately 30 J. This amount of heat deposited adiabatically into a fault of width 0.3 mm is sufficient to raise its temperature from 180 K to near the melting point but insufficient to cause melting. Arbitrarily, taking the duration of the event as 0.01 s and applying appropriate geometric factors for axisymmetric versus simple shear strain, we find, using the GSS flow law from Goldsby and Kohlstedt (2001), that at $T = 265$ K, the grain size required is roughly 10 nm (the calculations are shown in Table S3 along with a link to the table in worksheet format). This is obviously a rough and not necessarily conservative estimate, and while the calculated grain size is exceedingly small, it is not beyond the realm of possibility (Meyers et al., 2006). Alternatively, by the thermal softening model of Renshaw and Schulson (2017) wherein transformational superplastic weakening accompanies temperature rise to near melting, fault propagation is effected through cyclic episodes of strain concentration and grain size reduction. Whether by GSS or cyclic plastic faults, either mechanism also explains why the sample returns to full strength after faulting, if we assume substantial grain growth from nanometer size occurred in the moments after faulting. The images in Figure 9 cannot resolve this particular question because grain growth during handling at even warmer temperature (to 220 K) would likely have erased any signs of nanometer grains that might have existed.

It is possible to detect signs of ice I \rightarrow II phase change even at very low concentrations when ice II is expressed as local topographic depressions on the outer surface of samples and is replicated in microscopic detail as local bumps on the inside of the indium jacket. Such topography can be retained when the sample is cooled to <150 K before depressurization, which preserves the ice II in metastable form. Kirby et al. (1991, 1992) were able to show convincingly based on powder X-ray diffraction (Figure 2 in Kirby et al., 1992) and jacket replicas that some ice II was present in at least some of their plastically faulted samples. We have more recently reexamined the jacket replicas of samples run earlier. The jacket from plastically faulted run 273 (Figure 10) shows the fault trace along

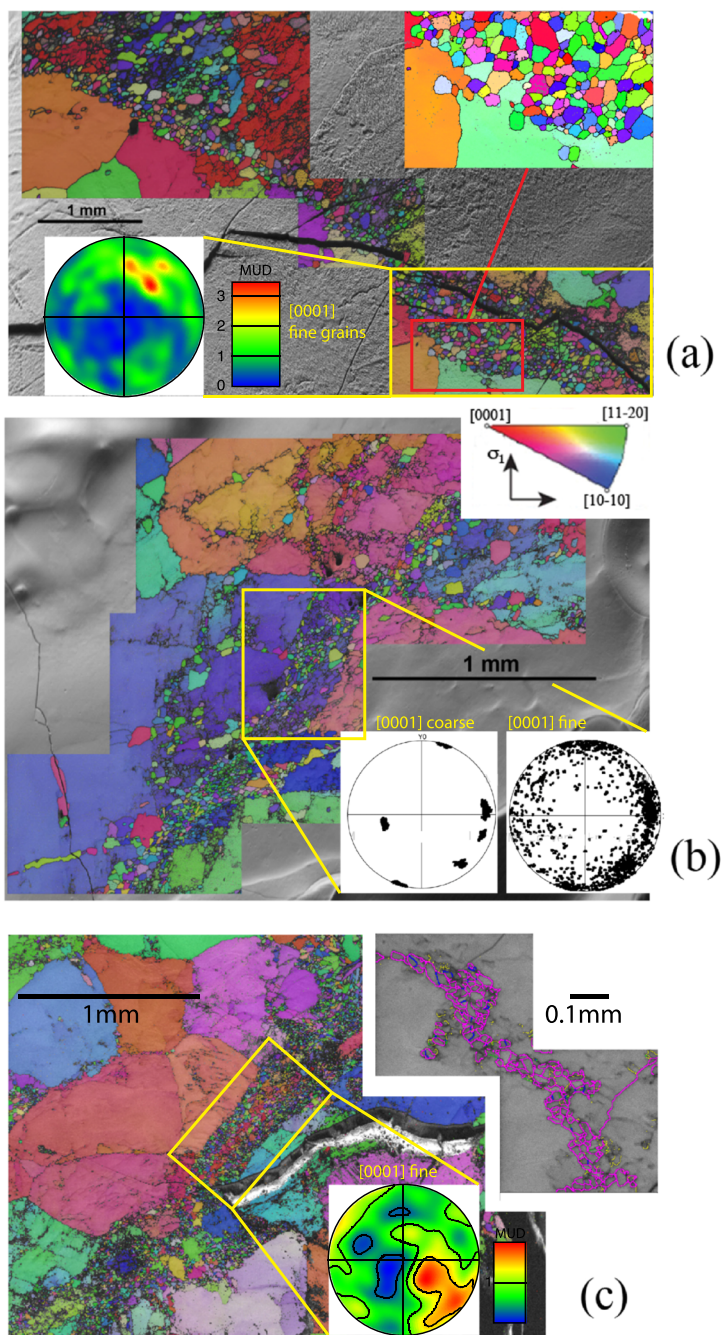


Figure 9. Structures observed in SEM-EBSD in the fault zones of three plastically faulted samples. Loading direction is vertical in all images. All EBSD data are shown as inverse pole figures (unless stated) with color indicating the crystal orientation in the loading direction, as shown in the legend at top right of (b). All stereonets are lower hemisphere equal area projections, with colors indicating distribution of grain orientations as a multiple of uniform distribution (MUD). (a) Run 671, failed at low T (105 K) and relatively high σ_{ult} (161 MPa), with macroscopic fault intersecting end cap (Figure 4). Inset shows microstructural detail of the area outlined in red. The contoured c -axis figure is from fine grains in the area outlined in yellow. (b) Run 724, failed at 180 K in multiple events near $\sigma_{ult} = 100$ MPa. External appearance suggests multiple fracture planes (Figure 4) of which this may be one. The ~2.5-mm length of fracture intersected here has a width of 0.05–0.2 mm. Fine grains surrounding some of the large original grains suggest recrystallization of highly strained regions near grain boundaries, a process characteristic of ductile flow. Coarse and fine-grained c -axis figures for the area outlined in yellow are shown. It is impossible to determine if this recrystallization played a role in fracture initiation or if it is a passive result of the violent fault displacement event. (c) Run 730, failed in a single event at 195 K. Inset at top right shows a structure from above and left of the main figure. This is a boundary map with yellow boundaries between 2° and 5°, green between 5° and 10°, blue between 10° and 20°, and purple greater than 20° of misorientation. Inset at center shows the c -axis pattern from fine grains in the yellow boxed area; red grains interpreted as inherited from the host larger grains are excluded from the data in this stereonet.

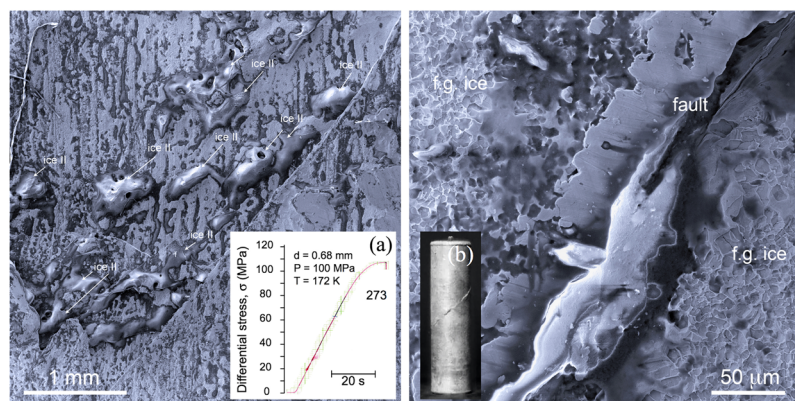


Figure 10. Indium jacket replica of outer cylindrical surface of plastically faulted sample 273 at 172 K and recovered at low temperature before depressurization to preserve ice II, as viewed in SEM. Smoothly outlined domains of positive topography are replicated locations of ice II on the sample surface; several examples are pointed out and labeled “ice II.” The chart record (inset a) shows a pronounced ductile precursor with a lag time of 19 s and a ductile strain of 0.006 prior to failure, which occurred virtually at the top of the yield curve, with faulting on a single plane inclined at 45° to σ_1 (inset b). Note also the fine-grained zone bordering the fault, labeled “f.g. ice.” The ice II domains appear to be elongated parallel to the trace of the fault, which is also the direction of maximum shear stress (left-hand micrograph). Ice II domains directly bordering the fault with no ice II on the opposing side fault (the fault offset of 0.5 mm or less, Figure 4, is well within the left-hand image) are near proof they postdate the fault. Right-hand micrograph is a higher magnification view of a different location along the fault. Note here that the ice II exists on both sides of the fault but does not itself appear to be faulted. The fault offset is approximately 0.5 mm, thus greater than the length of the fault trace in the right-hand image.

the fault, more in keeping with a uniaxial stress state and consistent with creation prior to faulting. The lineations themselves indicate interactions between neighboring inclusions that cause subsequent neighbors to form at a favored distance and direction, perhaps influenced by the direction of maximum shear stress. Thus, ice II inclusions that predate faulting and contribute to precursive strain (Figure 11a) and those that form after faulting (Figure 10) may both appear in faulted samples. Similarly to those in Figure 11a, ice II inclusions in arrays at various orientations also appear in unfaulted samples partially transformed under differential stress, such as run 292 from Kirby et al. (1991), shown in Figure 11b. Were several domains of aligned inclusions to develop on common planes of maximum shear, a jacket replica might be expected to show domains of lineations striking at orientations of 0° to 45° from horizontal and perhaps curving or splaying as is seen in Figure 11b.

4. Discussion

Our results reject the hypothesized exclusivity of transformational faulting as the mechanism for plastic faulting. The appearance of plastic faulting in ice II at 110 K, for which no available phase transformation exists, may be the most direct evidence of this. Load-displacement curves preceding brittle (plastic faulting) and ductile failure at $T \geq 160$ K are almost indistinguishable (Figure 7). Common patterns in behavior of plastic faulting and bulk I-II phase transformation are few (Figure 8). One serious inconsistency with the requirement for phase transformation is the absence of a convincing connection to plastic faulting in the one setting where evidence of such a connection would be most expected: when bulk I \rightarrow II transformation is occurring concurrently. The simplest interpretation of the observations taken together is that bulk phase transformation and plastic faulting run concurrently but independently.

How then is plastic faulting initiated? Assuming that in most instances, it is an expression of adiabatic shear instability, what is the origin of the first point of criticality, the nucleus of soft material that triggers the instability? The question applies whether or not the trigger is a load instability (i.e., the result of strain softening) or a gradually rising temperature (i.e., an insufficient rate of diffusion of heat). The promotion of an atomic-scale heterogeneity to an incipient point of instability (through, e.g., phase transformation, melting, critical grain-size reduction [Renshaw & Schulson, 2017; Semiatin et al., 1984], unblocking of lattice defects [Armstrong et al., 1982; Renshaw & Schulson, 2004; J. Weiss & Marsan, 2003], or other process) is at its

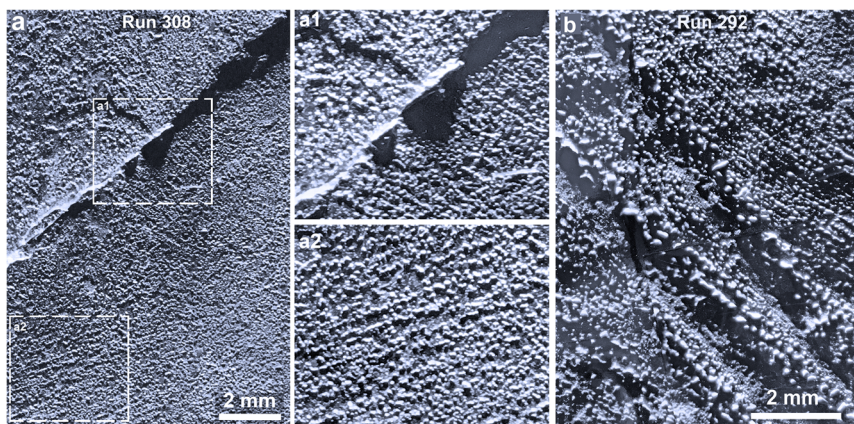


Figure 11. Indium jacket replicas of outer cylindrical surfaces of (a) faulted run 308 (200 MPa, 159 K, $\varepsilon = 0.002$) and (b) partially transformed run 292 (300 MPa, 158 K, $\varepsilon = 0.078$) as viewed optically at reflected grazing illumination, compression direction vertical. Both samples were quenched in liquid nitrogen before depressurization to preserve ice II. The long linear feature at 45° in (a) is the fault trace, and the small bright features are replicated locations of ice II inclusions. Ice II inclusions interact to form arrays, and domains of such arrays can be seen with lineations at various angles with respect to the fault trace, consistent with formation prior to faulting (see text). White outlined boxes in (a) are enlarged in (a1) and (a2). Run 292 (b) shows extensive development of ice II inclusions into preferentially oriented domains despite the sample never having faulted.

origin a stochastic process. If that is the case, then the preternaturally (for rocks) small variance of location of the B-D crossover (Figures 5–7) suggests a process that is buffered from the extremes in local stress that can exist in polycrystalline materials under load or, invoking the statistical effect of large sampling on variance, that requires not simply one but many temporally and spatially correlated points of incipient action. The very few number of small faulting events (seen as blips on the load-displacement record, e.g., Figure 7) preceding through-going faulting, and the fact they occur only very close in stress to σ_{ult} , is consistent with this precision. Contrast this behavior with Coulombic faulting in rocks, where microfracturing events begin well below σ_{ult} and steadily increase in number up to the point of failure (Lockner et al., 1991).

One way to buffer the effects of local stress concentrations is to relieve those concentrations by local I-II phase transformation. An interesting consequence of buffering in this manner is that if transformation and plastic faulting are indeed independent in ice as our observations imply (at least in the region near 180 K), then the precision of the B-D crossover is peculiar to ice (or other materials with accessible phase transformations) and may not be a property of plastic faulting in general. On the other hand, if plastic faulting is triggered by an adiabatic process, since thermal diffusion is inherently less sensitive to local stress or structural heterogeneities, a narrow B-D crossover would be expected no matter what the material. The matter is not likely to be resolved soon. Since the B-D crossover in ice can only be studied near 180 K (Figure 3), it would have to be approached with another material.

Thermally activated high-temperature plastic deformation in crystalline materials is the expression of spatially and temporally correlated stochastic events at the lattice scale, in particular dislocation avalanches and clustering of dislocation networks (e.g., Weiss et al. (2000)), yet sample-to-sample variance in flow stress is typically small. Although we have concluded that plastic faulting can proceed in the absence of phase transformation, we may exploit the images in Figure 11 to show an example of the organization that spontaneous formation of ice II inclusions can produce. As the density of inclusions increases, larger scale heterogeneities develop (e.g., the domains seen in the images) rather more predictably in a manner of so-called self-organized criticality (e.g., Bak et al., 1989). For the present case, the scale at which a soft nucleus of critical size and shape forms is difficult to predict.

It is conceivable that there is a mechanism of heterogeneous phase transformation involved in transformational faulting in ice I that is different from the homogenous (bulk) transformation that has been known since the time of Tammann (1903). However, the distinction between phase transformation and local structural rearrangements occurring during severe plastic deformation probably becomes

blurred at finer and finer scale. The essential difference for the discussion here is that the “phase” created during severe plasticity exists only under conditions of severe plasticity, which then frees up all materials to plastic faulting, not simply those which happen to have a nearby melting curve or phase transformation.

5. Conclusions

Water ice has given us the best opportunity yet to isolate and study the nucleating mechanism of plastic faulting, a process with important links to deep earthquakes and other shear instabilities in crustal rocks. It is fairly well established outside of this work that the narrow shear zone forming a plastic fault is an adiabatic instability (thermal runaway) that results from the combined reduction of grain size caused by recrystallization under high stress and the rheologic weakening that follows grain-size reduction and temperature increase. Plastic faulting is nucleated by a zone of weak material of sufficient volume to become adiabatically unstable. The nucleus forms under increasing stress as the ice I structure breaks down locally (and perhaps briefly) to a weaker structure, eventually at a rate such that local points of breakdown are sufficiently dense to interact mechanically. Unresolved are the scale of the local structural breakdown, the nature of the breakdown, and the time scale of the process. What is clear is that points of potential breakdown are widely distributed, that is, large stress concentrations are not required, and that the breakdown itself is not exclusively a known phase transformation. The results here do not require and in many instances are inconsistent with phase transformation. According to this model, most or all materials should be capable of plastic faulting, yet it has been seen in the laboratory in only a handful of rock types, two of which, interestingly, are ices I and II.

The principal experimental findings informing this model are as follows:

- Plastic faulting in polycrystalline ice I occurs over a broad range of temperature and pressure, at least $20 \leq P \leq 250$ MPa and $77 \leq T \leq 235$ K. Ultimate strength at failure is largely independent of pressure (Figure 2) and weakly dependent on temperature (Figure 3) over these ranges. The fault itself is confined to a narrow plane oriented at 45° to the principal normal stress (Figure 1).
- Plastic faulting also occurs in ice II.
- Plastically faulted samples retain their full strength (Figure 4), provided that jacket integrity is maintained.
- The change of failure mode at 180 K from brittle (plastic faulting) to ductile (plastic flow) as mapped against applied strain rate is, within a factor of well under two in strain rate, a sharp changeover (Figures 5–7). Mixed mode failure has not been observed.
- Inelastic precursors appear prior to most instances of plastic faulting (Figure S2); they originate from the combined action of bulk phase transformation from ice I to ice II plus ordinary defect-based plasticity, with the former predominating at $T < 195$ K in most runs ending in brittle failure.
- Inelastic precursors to brittle failure are virtually indistinguishable from those of ductile failure on the basis of stress-time records (Figure 7).
- The fault zone imaged in EBSD after testing has a width of roughly 0.2 to 0.5 mm and is filled with fine-grained crystalline ice I of roughly 1- to 10- μm diameter (Figure 9).

Acknowledgments

This work was supported by NASA/Outer Planets Research Program Grant NNX13AK98G. EBSD work was supported by Marsden Fund (NZ) Grants UOO1716 and UOO052. Any use of trade, firm, or product names is for descriptive purposes only and does not imply endorsement by the U.S. Government. The manuscript benefitted enormously from reviews from C. McCarthy and C. Renshaw and from presubmission reviews from C. Morrow and B. Kilgore. The data used are listed in the figures, tables, hyperlinks within the tables, and supporting information. Those data may also be accessed in a single collection at <https://doi.org/10.6084/m9.figshare.c.4836714>.

References

- Armstrong, R. W., Coffey, C. S., & Elban, W. L. (1982). Adiabatic heating at a dislocation pile-up avalanche. *Acta Metallurgica*, 30(12), 2111–2116. <http://www.sciencedirect.com/science/article/pii/0001616082901316>
- Bachmann, F., Hfelscher, R., & Schaeben, H. (2011). Grain detection from 2d and 3d EBSD data—Specification of the MTEX algorithm. *Ultramicroscopy*, 111(12), 1720–1733. <https://doi.org/10.1016/j.ultramic.2011.08.002>
- Bak, P., Chen, K., & Creutz, M. (1989). Self-organized criticality in the “Game of Life”. *Nature*, 342(6251), 780–782. <https://doi.org/10.1038/342780a0>
- Bestmann, M., & Prior, D. J. (2003). Intragranular dynamic recrystallization in naturally deformed calcite marble: Diffusion accommodated grain boundary sliding as a result of subgrain rotation recrystallization. *Journal of Structural Geology*, 25(10), 1597–1613.
- Bridge, P. W. (1912). Water, in the liquid and five solid forms, under pressure. *Proceedings of the American Academy of Arts and Sciences*, 47, 441–558. <https://doi.org/10.2307/20022754>
- Burnley, P. C., Green, H. W. II, & Prior, D. J. (1991). Faulting associated with the olivine to spinel transformation in Mg_2GeO_4 and its implications for deep-focus earthquakes. *Journal of Geophysical Research*, 96, 425–443.
- Byerlee, J. D. (1967). Frictional characteristics of granite under high confining pressure. *Journal of Geophysical Research*, 72(14), 3639–3648.

- Byerlee, J. D. (1968). Brittle-ductile transition in rocks. *Journal of Geophysical Research*, 73(14), 4741–4750. <https://doi.org/10.1029/JB073i014p04741>
- Craw, L., Qi, C., Prior, D. J., Goldsby, D. L., & Kim, D. (2018). Mechanics and microstructure of deformed natural anisotropic ice. *Journal of Structural Geology*, 115, 152–166. <https://doi.org/10.1016/j.jsg.2018.07.014>
- Duretz, T., Schmalholz, S. M., & Podladchikov, Y. Y. (2015). Shear heating-induced strain localization across the scales. *Philosophical Magazine*, 95(28–30), 3192–3207. <https://doi.org/10.1080/14786435.2015.1054327>
- Durham, W. B., Heard, H. C., & Kirby, S. H. (1983). Experimental deformation of polycrystalline H₂O ice at high pressure and low temperature: Preliminary results. *Journal of Geophysical Research*, 88(S01), B377–B392. <https://doi.org/10.1029/JB088iS01p0B377>
- Durham, W. B., Kirby, S. H., Heard, H. C., Stern, L. A., & Boro, C. O. (1988). Water ice phases II, III, and V: Plastic deformation and phase relationships. *Journal of Geophysical Research*, 93(B9), 10,191–10,208. <https://doi.org/10.1029/JB093iB09p10191>
- Durham, W. B., Kirby, S. H., & Stern, L. A. (1997). Creep of water ices at planetary conditions: A compilation. *Journal of Geophysical Research, Planets*, 102(E7), 16293–16302. <https://doi.org/10.1029/97JE00916>
- Echelman, K., & Kamb, B. (1986). Rheology of ice II and ice III from high-pressure extrusion. *Geophysical Research Letters*, 13(7), 693–696. <https://doi.org/10.1029/GL013i007p00693>
- Evans, B., Fredrich, J. T., & Wong, T. F. (1990). The brittle-ductile transition in rocks: Recent experimental and theoretical progress. *The Brittle-Ductile Transition in Rocks, Geophys. Monogr. Ser.*, 56, 1–20. <https://doi.org/10.1029/GM056p0001>
- Fu, R., O'Connell, R. J., & Sasselov, D. D. (2010). The interior dynamics of water planets. *Astrophysical Journal*, 708(2), 1326–1334. <https://doi.org/10.1088/0004-637X/708/2/1326>
- Gammon, P. H., Klefte, H., & Clouter, M. J. (1983). Elastic constants of ice samples by Brillouin spectroscopy. *Journal of Physical Chemistry*, 87(21), 4025–4029. <https://doi.org/10.1021/j100244a004>
- Golding, N., Schulson, E. M., & Renshaw, C. E. (2012). Shear localization in ice: Mechanical response and microstructural evolution of P-faulting. *Acta Materialia*, 60(8), 3616–3631. <https://doi.org/10.1016/j.actamat.2012.02.051>
- Goldsby, D. L., & Kohlstedt, D. L. (2001). Superplastic deformation of ice: Experimental observations. *Journal of Geophysical Research*, 106(B6), 11,017–11,1030. <https://doi.org/10.1029/2000JB900336>
- Green, H. W. II, & Burnley, P. C. (1989). A new self-organizing mechanism for deep-focus earthquakes. *Nature*, 341(6244), 733–737. <https://doi.org/10.1038/341733a0>
- Griggs, D., & Handin, J. (1960). Observations on fracture and a hypothesis of earthquakes. In D. Griggs & J. Handin (Eds.), *Rock deformation* (pp. 347–364). New York: Geol Soc Am.
- Heard, H. C., Durham, W. B., Boro, C. O., & Kirby, S. H. (1990). A triaxial deformation apparatus for service at 77 \leq T \leq 273 K. In *The brittle-ductile transition in rocks, geophysical monograph 56* (pp. 225–228). Washington DC: American Geophysical Union.
- Hobbs, B. E., & Ord, A. (1988). Plastic instabilities: Implications for the origin of intermediate and deep focus earthquakes. *Journal of Geophysical Research*, 93(B9), 10,521–10,540. <https://doi.org/10.1029/JB093iB09p10521>
- Jiang, J., Britton, T. B., & Wilkinson, A. J. (2013). Mapping type III intragranular residual stress distributions in deformed copper polycrystals. *Acta Materialia*, 61(15), 5895–5904. <https://doi.org/10.1016/j.actamat.2013.06.038>
- Karato, S., Riedel, M. R., & Yuen, D. A. (2001). Rheological structure and deformation of subducted slabs in the mantle transition zone: implications for mantle circulation and deep earthquakes. *Physics of the Earth and Planetary Interiors*, 127(1–4), 83–108. [https://doi.org/10.1016/S0031-9201\(01\)00223-0](https://doi.org/10.1016/S0031-9201(01)00223-0)
- Kirby, S. H., Durham, W. B., Beeman, M. L., Heard, H. C., & Daley, M. A. (1987). Inelastic properties of ice Ih at low temperatures and high pressures. *J. de Physique*, 48, Supplement (Proc. VII Symposium on the Physics and Chemistry of Ice, Grenoble, France), 227–232.
- Kirby, S. H., Durham, W. B., & Stern, L. A. (1991). Mantle phase changes and deep-earthquake faulting in subducting slabs. *Science*, 252(5003), 216–225. <https://doi.org/10.1126/science.252.5003.216>
- Kirby, S. H., Durham, W. B., & Stern, L. A. (1992). The ice I \rightleftharpoons II transformation: Mechanisms and kinetics under hydrostatic and non-hydrostatic conditions. In N. Maeno & T. Honda (Eds.), *Physics and chemistry of ice* (pp. 456–463). Sapporo: Hokkaido Univ. Press.
- Kohlstedt, D. L., Evans, B., & Mackwell, S. J. (1995). Strength of the lithosphere: Constraints imposed by laboratory measurements. *Journal of Geophysical Research*, 100(B9), 17,587–17,602. <https://doi.org/10.1029/95JB01460>
- Kubo, T., Durham, W. B., Stern, L. A., & Kirby, S. H. (2006). Grain size-sensitive creep in ice II. *Science*, 311(5765), 1267–1269. <https://doi.org/10.1126/science.1121296>
- Kula, E., & DeSisto, T. (1966). Plastic behavior of metals at cryogenic temperatures. In *Plastic behavior of metals at cryogenic temperatures*.
- Li, J. X., Zheng, Y. C., Thomsen, L., Lapen, T. J., & Fang, X. D. (2018). Deep earthquakes in subducting slabs hosted in highly anisotropic rock fabric. *Nature Geoscience*, 11(9), 696–700. <https://doi.org/10.1038/s41561-018-0188-3>
- Lockner, D. A. (1995). Rock failure. In T. J. Ahrens (Ed.), *Rock physics and phase relations: A handbook of physical constants, ref. shelf vol. 3* (pp. 127–147). Washington, DC: AGU.
- Lockner, D. A., Byerlee, J. D., Kuksenko, V., Ponomarev, A., & Sidorin, A. (1991). Quasi-static fault growth and shear fracture energy in granite. *Nature*, 350(6313), 39–42. <https://doi.org/10.1038/350039a0>
- Lockner, D. A., Summers, R., Moore, D., & Byerlee, J. D. (1982). Laboratory measurements of reservoir rock from the Geysers geothermal field, California. *International Journal of Rock Mechanics and Mining Science and Geomechanics Abstracts*, 19(2), 65–80. [https://doi.org/10.1016/0148-9062\(82\)91632-1](https://doi.org/10.1016/0148-9062(82)91632-1)
- Mariani, E., Aslin, J., Covey-Crump, S., Dawson, K., Hansen, L., Wallis, D., & Wheeler, J. (2018). *The role of lattice defects in the localisation of strain at the grain-scale*. Paper presented at the EGU General Assembly Conference.
- McKinnon, W. B. (1998). Geodynamics of icy satellites. In B. Schmitt, C. De Bergh, & M. Festou (Eds.), *Solar system ices: Based on reviews presented at the International Symposium “Solar System Ices” held in Toulouse, France, on March 27–30, 1995* (pp. 525–550). Dordrecht: Springer Netherlands.
- Meade, C., & Jeanloz, R. (1991). Deep-focus earthquakes and recycling of water into the earth's mantle. *Science*, 252(5002), 68–72. <https://doi.org/10.1126/science.252.5002.68>
- Melosh, H. J. (1989). *Impact cratering: a geologic process*. New York: Oxford University Press.
- Meyers, M. A., Mishra, A., & Benson, D. J. (2006). Mechanical properties of nanocrystalline materials. *Progress in Materials Science*, 51(4), 427–556. <https://doi.org/10.1016/j.pmatsci.2005.08.003>
- Mishima, O., & Endo, S. (1980). Phase relations of ice under pressure. *The Journal of Chemical Physics*, 73(5), 2454–2456. <https://doi.org/10.1063/1.440396>

- Murr, L. E., Trillo, E. A., Pappu, S., & Kennedy, C. (2002). Adiabatic shear bands and examples of their role in severe plastic deformation. *Journal of Materials Science*, 37(16), 3337–3360. <https://doi.org/10.1023/A:1016541023502>
- Paterson, M. S. (1978). *Experimental rock deformation—The brittle field*. Berlin: Springer.
- Petrenko, V. F., & Whitworth, R. W. (1999). *Physics of ice*. Oxford: New York.
- Poirier, J. P. (1980). Shear localization and shear instability in materials in the ductile field. *Journal of Structural Geology*, 2(1-2), 135–142. [https://doi.org/10.1016/0191-8141\(80\)90043-7](https://doi.org/10.1016/0191-8141(80)90043-7)
- Poirier, J.-P., Sotin, C., & Peyronneau, J. (1981). Viscosity of high-pressure ice VI and evolution and dynamics of Ganymede. *Nature*, 292(5820), 225–227. <https://doi.org/10.1038/292225a0>
- Prior, D. J., Lilly, K., Seidemann, M., Vaughan, M., Becroft, L., Easingwood, R., et al. (2015). Making EBSD on water ice routine. *Journal of Microscopy*, 259(3), 237–256. <https://doi.org/10.1111/jmi.12258>
- Qi, C., Prior, D. J., Craw, L., Fan, S., Llorens, M. G., Griera, A., et al. (2019). Crystallographic preferred orientations of ice deformed in direct-shear experiments at low temperatures. *The Cryosphere*, 13(1), 351–371. <https://doi.org/10.5194/tc-13-351-2019>
- Regenauer-Lieb, K., & Yuen, D. A. (2003). Modeling shear zones in geological and planetary sciences: Solid- and fluid-thermal-mechanical approaches. *Earth-Science Reviews*, 63(3–4), 295–349. [https://doi.org/10.1016/S0012-8252\(03\)00038-2](https://doi.org/10.1016/S0012-8252(03)00038-2)
- Renshaw, C. E., & Schulson, E. M. (2001). Universal behavior in compressive failure of brittle materials. *Nature*, 412, 897–900. <https://doi.org/10.1038/35091045>
- Renshaw, C. E., & Schulson, E. M. (2004). Plastic faulting: Brittle-like failure under high confinement. *Journal of Geophysical Research - Solid Earth*, 109(B9), 10. <https://doi.org/10.1029/2003jb002945>
- Renshaw, C. E., & Schulson, E. M. (2017). Strength-limiting mechanisms in high-confinement brittle-like failure: Adiabatic transformational faulting. *Journal of Geophysical Research: Solid Earth*, 122, 1088–1106. <https://doi.org/10.1002/2016JB013407>
- Rist, M. A., Jones, S. J., & Slade, T. D. (1994). Microcracking and shear fracture in ice. *Annals of Glaciology*, 19, 131–137. <https://doi.org/10.3189/1994AoG19-1-131-137>
- Rist, M. A., & Murrell, S. A. F. (1994). Ice triaxial deformation and fracture. *Journal of Glaciology*, 40(135), 305–318. <https://doi.org/10.1017/S002214300007395>
- Rittel, D., Landau, P., & Venkert, A. (2008). Dynamic recrystallization as a potential cause for adiabatic shear failure. *Physical Review Letters*, 101(16), 165501. <https://doi.org/10.1103/PhysRevLett.101.165501>
- Rogers, H. C. (1979). Adiabatic plastic deformation. *Annual Review of Materials Science*, 9(1), 283–311. <https://doi.org/10.1146/annurev.ms.09.080179.001435>
- Rubie, D. C., & Ross, C. R. (1994). Kinetics of the olivine-spinel transformation in subducting lithosphere: Experimental constraints and implications for deep slab processes. *Physics of the Earth and Planetary Interiors*, 86(1-3), 223–243. [https://doi.org/10.1016/0031-9201\(94\)05070-8](https://doi.org/10.1016/0031-9201(94)05070-8)
- Sammonds, P. R., Murrell, S. A. F., & Rist, M. A. (1998). Fracture of multiyear sea ice. *Journal of Geophysical Research*, 103(C10), 21795–21815. <https://doi.org/10.1029/98JC01260>
- Schubert, G., Yuen, D. A., & Turcotte, D. L. (1975). Role of phase transitions in a dynamic mantle. *Geophysical Journal of the Royal Astronomical Society*, 42(2), 705–735. <https://doi.org/10.1111/j.1365-246x.1975.tb05888.x>
- Schubnel, A., Brunet, F., Hilairet, N., Gasc, J., Wang, Y. B., & Green, H. W. (2013). Deep-focus earthquake analogs recorded at high pressure and temperature in the laboratory. *Science*, 341(6152), 1377–1380. <https://doi.org/10.1126/science.1240206>
- Schulson, E. M. (1990). The brittle compressive fracture of ice. *Acta Metallurgica et Materialia*, 38(10), 1963–1976. [https://doi.org/10.1016/0956-7151\(90\)90308-4](https://doi.org/10.1016/0956-7151(90)90308-4)
- Schulson, E. M. (1999). The structure and mechanical behavior of ice. *JOM*, 51(2), 21–27. <https://doi.org/10.1007/s11837-999-0206-4>
- Schulson, E. M. (2002). Compressive shear faults in ice: Plastic vs. Coulombic faults. *Acta Materialia*, 50(13), 3415–3424. [https://doi.org/10.1016/S1359-6454\(02\)00154-4](https://doi.org/10.1016/S1359-6454(02)00154-4)
- Semiatin, S. L., Staker, M. R., & Jonas, J. J. (1984). Plastic instability and flow localization in shear at high rates of deformation. *Acta Metallurgica*, 32(9), 1347–1354. [https://doi.org/10.1016/0001-6160\(84\)90080-4](https://doi.org/10.1016/0001-6160(84)90080-4)
- Singer, K. N., McKinnon, W. B., & Nowicki, L. T. (2013). Secondary craters from large impacts on Europa and Ganymede: Ejecta size-velocity distributions on icy worlds, and the scaling of ejected blocks. *Icarus*, 226(1), 865–884. <https://doi.org/10.1016/j.icarus.2013.06.034>
- Stern, L. A., Durham, W. B., & Kirby, S. H. (1997). Grain-size-induced weakening of H₂O ices I and II and associated anisotropic recrystallization. *Journal of Geophysical Research*, 102(B3), 5313–5325. <https://doi.org/10.1029/96JB03894>
- Tammann, G. (1903). *Kristallizieren und Schmelzen*. Leipzig: Barth.
- Vaughan, M. J., van Wijk, K., Prior, D. J., & Bowman, M. H. (2016). Monitoring the temperature-dependent elastic and anelastic properties in isotropic polycrystalline ice using resonant ultrasound spectroscopy. *The Cryosphere*, 10(6), 2821–2829. <https://doi.org/10.5194/tc-10-2821-2016>
- Wallis, D., Hansen, L. N., Britton, T. B., & Wilkinson, A. J. (2019). High-angular resolution electron backscatter diffraction as a new tool for mapping lattice distortion in geological minerals. *Journal of Geophysical Research: Solid Earth*, 124(7), 6337–6358. <https://doi.org/10.1029/2019JB017867>
- Warren, J. M., & Hirth, G. (2006). Grain size sensitive deformation mechanisms in naturally deformed peridotites. *Earth and Planetary Science Letters*, 248(1-2), 438–450. <https://doi.org/10.1016/j.epsl.2006.06.006>
- Weiss, J., Lahaie, F., & Grassé, J. R. (2000). Statistical analysis of dislocation dynamics during viscoplastic deformation from acoustic emission. *Journal of Geophysical Research*, 105(B1), 433–442. <https://doi.org/10.1029/1999JB900312>
- Weiss, J., & Marsan, D. (2003). Three-dimensional mapping of dislocation avalanches: Clustering and space/time coupling. *Science*, 299(5603), 89–92. <https://doi.org/10.1126/science.1079312>
- Wheeler, J. (2014). Dramatic effects of stress on metamorphic reactions. *Geology*, 42(8), 647–650. <https://doi.org/10.1130/G35718.1>